https://dx.doi.org/10.1016/j.snb.2020.128075

Rational Design of Red Fluorescent and Selective G-quadruplex DNA Sensing Probes: The Study of Interaction Signaling and the Molecular Structural Relationship Achieving High Specificity

Bo-Xin Zheng,[a] Wei Long,[a] Yi-Han Zhang,[a] Xuan-He Huang,[a] Cui-Cui Chen,[a]
Dong-Xiao Zhong,[a] Meng-Ting She,[a] Ze-Xin Chen,[a] Dong-Peng Cai,[a] Yu-Jing Lu,[*,a] and
Wing-Leung Wong[*,b]

[a] School of Biomedical and Pharmaceutical Sciences, Guangdong University of Technology, Guangzhou 510006, P. R. China.
[b] The State Key Laboratory of Chemical Biology and Drug Discovery, Department of Applied Biology and Chemical Technology, The Hong Kong Polytechnic University, Hung Hom, Kowloon, Hong Kong, China.

* Corresponding author
E-mail: luyj@gdut.edu.cn;
E-mail: wing.leung.wong@polyu.edu.hk

Graphical abstract

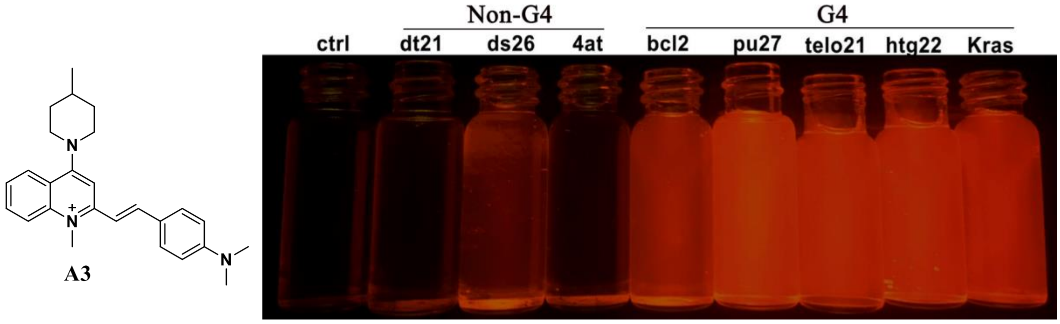

Abstract

Red fluorescent G-quadruplex DNA selective organic binding probe is relatively underdeveloped. In the present study, we designed a series of new fluorescent probes that exhibit large Stokes shift (112-131 nm), high quantum yield (up to 0.56), robust against photo-bleaching and high selectivity towards quadruplex structures of c-MYC and telomere DNA with strong binding affinity. The discrimination ability of the probes towards G-quadruplex structures against single-/double-stranded DNA or RNA was investigated by analyzing their structural property with respect to their binding specificity. From the sensing application of the probe targeting pu27, an excellent linear relationship ($R^2 = 0.9997$) with respect to the pu27-**A3** interaction signal was observed. The LOD was found down to 4.0 nM, which is superior to thiazole orange dye. The probe is able to realize real-time fluorescence visualization in aqueous, PAGE staining and live cell imaging. In addition, from the immunofluorescence analysis using the probe and BG4 antibody, the **A3** foci and BG4 staining co-localized well in PC3 cells, which suggest that the probe is G-quadruplex selective and useful for visualizing G-quadruplex DNA structures in live cells. Cytotoxicity assays also demonstrated that the probe has low cytotoxicity against both PC3 cancer cells and 16HBE normal cells.

Keywords: Red fluorescent quadruplex DNA probes, DNA structure discrimination, c-myc DNA recognition, BG4 antibody co-localization, live cell imaging.

1. Introduction

Nucleic acids are the vital genetic material of life in nature and play an important role in the growth, development, reproduction, heredity and variation of organisms [[1]]. There are two types of nucleic acids, ribonucleic acid (RNA) and deoxyribonucleic acid (DNA). It has been known that nucleic acids can form a variety of secondary structures. In addition to the classical double helix structure, they can also form other non-canonical structures [[4]]. Among various structures, the G-quadruplex (G4) structure has been an attractive research area since its first discovery in 1960s [[8]]. The G4 structure is typically formed in the region rich in guanine and its basic structural unit is G-tetrad, which is formed by Hoogsteen hydrogen bond through four guanine residues in the same plane. Two or more these G-tetrad units are able to stack together via π-π stacking to form a more stable nucleic acid structure with its central channel coordinated with some potassium or sodium ions [[9]]. Bioinformatics indicates that there are approximately 400,000 possible G4 formation sequences in the human genome [[12]]. In the key regulatory regions of human genomes, such as telomeres, proto-oncogene promoter regions, non-transcribed mRNA regions and ribosomal DNA regions, there are many G-rich sequences, which can form G-quadruplexes under certain conditions [[2][14]]. Some recent studies have also found that G4 structures can regulate the physiological activities in living systems, such as G-rich DNA sequences forming G4 structures to influence gene expression during replication or transcription [[15]]. In addition, G4 structures seem to be closely related to tumor [[18]].

To study these vital G4-DNA biomolecules *in vitro* or in live cells for their structural properties and biofunctions, the development of stable, high quantum yield, and selective fluorescent probes for rapid detection and real-time visualization is very important [[19]24]. With the use of merit fluorescent binding probes, the investigation of their structural folding dynamics, biofunctions and their real-time location of appearance *in vivo* becomes possible. In recent years, it has been a hot research field to search for new types of G4-specific fluorescent probes. A large number of fluorescent probes targeting G4-structures have been reported, such as thioflavin T [[25]], naphthalene diimide [[26]], thiazole orange derivatives [[27]], triphenylamine [[28]], quinolinium [[29]] and tetraarylimidazole [[30]]. Despite the G4-fluorescent binding probe development demonstrated great improvement in the binding affinity and sensitivity performance, most reported probes show poor discrimination between different G4 and i-motif structures against the dominated double-stranded DNA and thus they cannot specifically identify G4-strands, which is less feasible for the study of biological process involving G4-DNA molecules *in vivo*.

Currently, many researchers have made great efforts to develop highly G4-specific fluorescent probes to overcome these weak points encountered in the current fluorescent probe development. **E36** is a styryl compound that is a well studied RNA probe; however, its binding ability with RNA is weak [[31]]. Our group has also attended to modify the molecular scaffold of **E36** to enhance the recognition specificity and binding affinity towards RNA by introducing amino side group into the quinolinium core unit [[32]]. In the present study, in the molecular design, we retained the amino side group attached to the quinolinium but tuning the rigidity of the amino groups on the core unit to study their structure and specificity relationship targeting G4-DNA molecules. A series of new and near-infrared fluorescence probes with high quantum yields in aqueous medium under physiological conditions were developed and one of the analogues was found much more selectively in the detection of G4-DNAs (c-myc and telomere DNA) than single-/double-stranded DNAs and RNA. The *in vitro* and *in vivo* experimental results demonstrate the advantages of the new probes used in bio-analytical and live cell imaging applications.

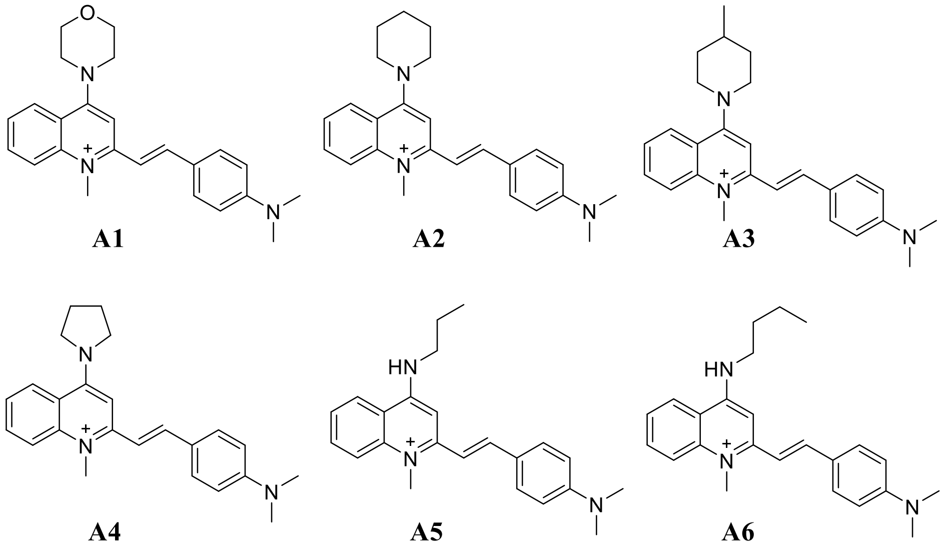

Scheme 1. The chemical structures of **A1-A6**

2. Experimental Section

2.1 Materials

In the present study, all chemicals and reagents were purchased from commercial in AR grade and were used without further purifications. The polyacrylamide gel materials were purchased from Shanghai Generay Biotechnology Co., Ltd. Tris-buffer was purchased from Aladdin. PBS was purchased from Thermo Fisher Scientific. The 1% Triton X-100 was purchased from Beijing Dingguo Changsheng Biotechnology Co., Ltd. All the oligonucleotides were synthesized and purified by Thermo Fisher Scientific and their sequences were listed in T**able S1**.

2.2 Synthesis and characterization

*2.2.1 Preparation of intermediate **a***

The synthesis of intermediate **a** was followed the reported procedures [[32]]. Briefly, 4-chloro-2-methylquinoline (1.5 mmol) and iodomethane (4.5 mmol) were added to a closed pressure reactor and then the compounds were dissolved with tetramethylene sulfone (6 mL). The mixture was heated at 60 °C and reacted for 2 h. After reaction, the mixture was cooled to room temperature and then ethyl acetate (15 mL) was added to precipitate the crude products. The pure products were obtained by recrystallization of ethanol.

*2.2.2 Preparation of new compounds **A1-A6***

Intermediate **a** (0.2 mmol), a selected amine (morpholine, piperidine, 4-methylpiperidine, pyrrolidine, propylamine and *N*-butyl amine) (0.6 mmol) and 4-dimethylaminobenzaldehyde (0.4 mmol) were added to a flask. The compounds were dissolved with *n*-butanol (4 mL). The mixture was stirred and refluxed at 80 °C for 8 h. When the reaction was finished, the mixture was cooled to room temperature and then ethyl acetate (10 mL) was added. After standing for 30 min, the crude products were obtained by suction filtration. The target compounds were obtained by recrystallization with ethanol. The compounds were characterized with ^{1}H, ^{13}C NMR, and HRMS.

*2.2.3 (E)-2-(4-(dimethylamino)styryl)-1-methyl-4-morpholinopyridin-1-ium (**A1**)*

Compound **A1** was isolated as an air stable brown solid with 87.6 % yield. ^{1}H NMR (400 MHz, DMSO-*d₆*): δ 8.28 (d, *J* = 8.8 Hz, 1H), 8.16 (d, *J* = 8.8 Hz, 1H), 8.00 (t, *J* = 7.8 Hz, 1H), 7.94 (d, *J* = 15.6 Hz, 1H), 7.76 (d, *J* = 8.8 Hz, 2H), 7.72 (t, *J* = 7.8 Hz, 1H), 7.50 (s, 1H), 7.41 (d, *J* = 15.6 Hz, 1H), 6.81 (d, *J* = 8.8 Hz, 2H), 4.23 (s, 3H), 3.91 (t, *J* = 7.1 Hz, 4H), 3.70 (t, *J* = 7.1 Hz, 4H), 3.05 (s, 6H). ^{13}C NMR (101 MHz, DMSO-*d₆*): δ 159.42, 155.46, 152.59, 145.49, 141.24, 133.98, 131.26, 126.81, 126.61, 123.05, 120.29, 119.65, 113.53, 112.26, 105.19, 66.29, 52.47, 38.48. HRMS m/z: calcd for $C_{24}H_{28}N_3O^+$, $[M-I]^+$ = 374.2227, found 374.2260.

*2.2.4 (E)-2-(4-(dimethylamino)styryl)-1-methyl-4-(piperidin-1-yl)pyridin-1-ium (**A2**)*

Compound **A2** was isolated as an air stable brown solid with 89.7 % yield. ^{1}H NMR (400 MHz, DMSO-*d₆*): δ 8.24 (d, *J* = 8.8 Hz, 1H), 8.07 (d, *J* = 8.0 Hz, 1H), 7.98 (t, *J* = 7.6 Hz, 1H), 7.88 (d, *J* = 15.6 Hz, 1H), 7.75 (d, *J* = 8.8 Hz, 2H), 7.71 (t, *J* = 7.8 Hz, 1H), 7.43 (s, 1H), 7.38 (d, *J* = 15.6 Hz, 1H), 6.80 (d, *J* = 9.2 Hz, 2H), 4.19 (s, 3H), 3.67 (t, *J* = 5.1 Hz, 4H), 3.04 (m, 6H), 1.83 (m, 4H), 1.76 (s, 2H). ^{13}C NMR (101 MHz, DMSO-*d₆*): δ 159.79, 155.04, 152.46, 144.76, 141.31, 133.86, 131.08, 126.84, 126.30, 123.11, 120.33, 119.50, 113.77, 112.25, 104.65, 53.23, 38.30, 25.88, 24.05. HRMS m/z: calcd for $C_{25}H_{30}N_3^+$, $[M-I]^+$ = 372.2434, found 372.2482.

*2.2.5 (E)-2-(4-(dimethylamino)styryl)-1-methyl-4-(4-methylpiperidin-1-yl)pyridin-1-ium (**A3**)*

Compound **A3** was isolated as an air stable brown solid with 90.4 % yield. ^{1}H NMR (400 MHz, DMSO-*d₆*): δ 8.23 (d, *J* = 12.0 Hz, 1H), 8.07 (d, *J* = 8.0 Hz, 1H), 7.98 (t, *J* = 8.0 Hz, 1H), 7.88 (d, *J* = 8.0 Hz, 1H), 7.75 (d, *J* = 8.0 Hz, 2H), 7.70 (t, *J* = 8.0 Hz, 1H), 7.44 (s, 1H), 7.38 (d, *J* = 16.0 Hz, 1H), 6.80 (d, *J* = 8.0 Hz, 2H), 4.19 (s, 3H), 4.06 (t, *J* = 9.4 Hz, 2H), 3.28 (t, *J* = 9.4 Hz, 2H), 3.04 (s, 6H), 1.86 (m, 2H), 1.77 (m, 1H), 1.48 (m, 2H), 1.03 (d, *J* = 8.0 Hz, 3H). ^{13}C

NMR (101 MHz, DMSO-d_6): δ 159.64, 155.00, 152.46, 144.74, 141.30, 133.86, 131.08, 126.87, 126.29, 123.11, 120.33, 119.49, 113.75, 112.24, 104.71, 52.50, 38.29, 34.03, 30.49, 21.96. HRMS m/z: calcd for $C_{26}H_{32}N_3^+$, $[M-I]^+$ = 386.2591, found 386.2662.

*2.2.6 (E)-2-(4-(dimethylamino)styryl)-1-methyl-4-(pyrrolidin-1-yl)quinolin-1-ium (**A4**)*

Compound **A4** was isolated as an air stable orange solid with 90.5 % yield. 1H NMR (400 MHz, DMSO-d_6): δ 8.49 (d, J = 7.6 Hz, 1H), 8.13 (d, J = 8.4 Hz, 1H), 7.96 (m, 1H), 7.71 (d, J = 9.2 Hz, 1H), 7.68 (d, J = 2.4 Hz, 2H), 7.64 (m, 1H), 7.31 (d, J = 15.6 Hz, 1H), 6.97 (s, 1H), 6.78 (d, J = 9.2 Hz, 2H), 4.07 (s, 3H), 4.00 (t, J = 7.1 Hz, 4H), 3.02 (s, 6H), 2.05 (m, 4H). ^{13}C NMR (101 MHz, DMSO-d_6): δ 154.51, 153.31, 152.08, 142.60, 141.26, 133.56, 130.53, 127.54, 125.11, 123.20, 118.73, 118.61, 114.57, 112.23, 99.77, 53.77, 38.05, 25.71. HRMS m/z: calcd for $C_{24}H_{28}N_3^+$, $[M-I]^+$ = 358.2278, found 358.2278.

*2.2.7 (E)-2-(4-(dimethylamino)styryl)-1-methyl-4-(propylamino)quinolin-1-ium (**A5**)*

Compound **A5** was isolated as an air stable brown solid with 88.4 % yield. ^{1}H NMR (400 MHz, DMSO-d_6): δ 8.83 (t, J = 5.2 Hz, 1H), 8.52 (d, J = 8.0 Hz, 1H), 8.16 (d, J = 8.8 Hz, 1H), 7.99 (t, J = 7.6 Hz, 1H), 7.73 (m, 2H), 7.70 (m, 2H), 7.34 (d, J = 15.6 Hz, 1H), 7.05 (s, 1H), 6.79 (d, J = 9.2 Hz, 2H), 4.10 (s, 3H), 3.61 (dd, J = 12.9, 6.6 Hz, 2H), 3.02 (s, 6H), 1.78 (m, 2H), 1.02 (t, J = 7.2 Hz, 3H). ^{13}C NMR (101 MHz, DMSO-d_6): δ 155.36, 153.76, 152.15, 143.31, 140.02, 134.02, 130.67, 126.34, 123.70, 123.16, 119.26, 117.72, 114.60, 112.20, 96.41, 45.05, 37.77, 21.72, 11.94. HRMS m/z: calcd for $C_{23}H_{28}N_3^+$, $[M-I]^+$ = 346.2278, found 346.2278.

*2.2.8 (E)-4-(butylamino)-2-(4-(dimethylamino)styryl)-1-methylquinolin-1-ium (**A6**)*

Compound **A6** was isolated as an air stable brown solid with 88.7 % yield. ^{1}H NMR (400 MHz, DMSO-d_6): δ 8.81 (t, J = 8.0 Hz, 1H), 8.52 (d, J = 8.0 Hz, 1H), 8.16 (d, J = 8.8 Hz, 1H), 7.98 (t, J = 8.0 Hz, 1H), 7.74 (s, 1H), 7.71 (d, J = 9.2 Hz, 3H), 7.34 (d, J = 15.6 Hz, 1H), 7.04 (s, 1H), 6.79 (d, J = 8.8 Hz, 2H), 4.09 (s, 3H), 3.63 (m, 2H), 3.02 (s, 6H), 1.74 (m, 2H), 1.46 (m, 2H), 0.97 (t, J = 7.4 Hz, 3H). ^{13}C NMR (101 MHz, DMSO-d_6): δ 155.35, 153.69, 152.16, 143.30, 140.01, 134.01, 130.66, 126.35, 123.71, 123.15, 119.26, 117.73, 114.62, 112.21, 96.40, 43.19, 37.77, 30.43, 20.19, 14.26. HRMS m/z: calcd for $C_{24}H_{30}N_3^+$, $[M-I]^+$ = 360.2434, found 360.2434.

2.3 Methods

2.3.1 Fluorescence measurements and fluorescence quantum yield

The UV-Vis and fluorescence spectra were recorded with Lambda 25 Spectrophotometer (Perkin Elmer) and LS-45 fluorescence spectrometer (Perkin Elmer), respectively. The slit width of the colorimetric dish is 1 mm and optical diameter is 10 mm.

The calculation of fluorescence quantum yields was based on the equation: $\Phi_x = \Phi_{ST} (Grad_x / Grad_{ST}) (\eta^2_x / \eta^2_{ST})$. In the equation, the subscript ST represents standard, the subscript X represents test, Φ represents fluorescence quantum yields, Grad represents gradient from the plot of integrated fluorescence intensity versus absorbance, and η represents refractive index of the solvent. In the present study, the standard used was fluorescein (1 % NaOH ethanol, $\Phi = 0.85$).

2.3.2 The limit of detection (LOD)

The limit of detection (LOD) of the compounds were obtained by fluorescence titration and estimated based on the calculation formula: $LOD = K(S_b/m)$. In the equation, S_b is the standard deviation of the blank multiple measurements ($n = 20$), and m is the slope of the calibration curve, which represents the sensitivity of this method. In addition, according to the International Union of Pure and Applied Chemistry (IUPAC), K value is generally taken to be 3.

2.3.3 Circular dichroism (CD) and melting point test

The CD spectra were performed on a Chirascan spectrophotometer (Applied Photophysics). During the experiment, a quartz cuvette with a length of 1 mm was used to record the spectrum in a wavelength range of 220 to 340 nm with a 1 nm bandwidth, a 1 nm step and 0.5 s per point. The melting point test was set at a fixed wavelength, while gradually increasing the temperature from 25 to 95 °C, 1 nm step size, and 5 s per point.

2.3.4 NMR titration

Experiments were performed on 600 MHz Bruker spectrometers at 25 °C. The G4 samples for ^{1}D NMR were prepared in a phosphate buffer (25 mM KH_2PO_4, 70 mM KCl, 10 % D_2O, pH 7.4) with Htg24 G4 and pu22 G4, respectively. The final concentration of G4-DNA was 300 µM and was titrated with compound **A3**. The final concentration of **A3** was 600 µM.

2.3.5 Native PAGE experiment conditions

The gel electrophoresis was based on 30 % (29:1) polyacrylamide gels with a size of 160 x 140 x 0.75 mm. The oligonucleotides used in the experiment included various single-, duplex-and quadruplex-forming oligonucleotides, with a fixed concentration of 5 mM, and they were run in 1 x TBE buffer (80 mM Tris-borate, 2 mM EDTA, pH 8.3). The experimental parameters were as follows: temperature = 0 °C, voltage = 110 V, time = 4 h. Finally, the removed gel was stained with compound **A3** (5 mM) in 1 x TBE for 20 min. Meanwhile, a commercial **SYBR Gold** (1 mM) was used to stain another gel as a control [[33]].

2.3.6 Living cells staining experiment

PC3 cells were cultured in confocal dishes for 24 h. After the removal of medium, the confocal dishes were washed with pre-cooled PBS for six times. After washing, the cells were fixed by pre-cooled 99 % methanol (-4 °C) for 1 min. Then, the sample was washed with methanol and followed with pre-cooled PBS for 6 times. To the PC3 cells sample **A3** (10 μM) was added and then incubated at 37 °C for 1 h. After that, the cells were washed 6 times with pre-cooled PBS and incubated with **DAPI** (5 μg/mL) at 37 °C for 30 min. Finally, the confocal dishes were washed with pre-cooled PBS and then it was observed under confocal microscope. The excitation wavelengths were 402 nm for **DAPI** and 488 nm and 560 nm for **A3**, respectively [[34]]. The digital images were then recorded on Olympus IX71 inverted fluorescence microscope and confocal laser scanning microscopy (ZEISS LSM 800 with Airscan).

2.3.7 DNase and RNase digestion tests

On the basis of living cells staining experiment, 1 mL DNase (Sigma, 50 μg/mL) and RNase (GE, 50 μg/mL) were added to the confocal dishes respectively and then the sample was cultured at 37 °C for 3 h under 5 % CO_2. After that, the solution was removed from the confocal dishes and the sample was washed with pre-cooled PBS for 6 times [[35]]. Finally, the digital images were recorded on Olympus IX71 inverted fluorescence microscope.

2.3.8 Immunofluorescence experiment

PC3 cells were cultured in confocal dishes. When the cells grew to a certain number, the medium was removed and the cells were fixed in 4 % paraformaldehyde/PBS for 15 min. Then, PC3 cells were permeabilized with 0.1 % Triton-X 100/PBS at 37 °C for 30 min and then were blocked with 5 % goat serum/PBS for 3 h. After pretreatment, the immunofluorescence was detected by following the standard method: Briefly, PC3 cells were incubated with Mouse anti-DNA G-quadruplex Antibody (**BG4**, absolute) at 37 °C for 3 h [[36]]. Then, the sample was washed with blocking buffer for 6 times. Dylight 405-AffinityPure Goat Anti-Mouse IgG H&L (Jackson) was added to the sample for incubation for 3 h and followed by adding 10 μM **A3** for 1 h incubation. Finally, Zeiss LSM 800 microscope was used to record digital images. Zen software was used for the analysis.

2.3.9 MTT assay

Both cancer cells PC3 and normal cells 16HBE cells were used in the MTT experiments. The cells were cultured on 96-well plates with a density of 8000 cells per well approximately. The culture medium was 1640 (containing 10 % fetal bovine serum and 0.5 % bivalent antibody) and the culture condition was set at 37 °C and 0.5 % CO_2. After cultured for 48 h, the 96-well plate was washed three times with pre-cooled PBS and then PC3 cells and 16HBE cells were treated with **A3** solutions at different concentrations (0, 0.25, 0.5, 1, 5, and 10 μM) for 24 h, respectively. After culture, the medium was decanted and 5 mg/mL of MTT solution, 200 μL per well, was added to the sample and then incubated for 4 h in dark. Then, the MTT solution was decanted and DMSO (100 μL per well) was added to ensure the deck adhering to 96-well plate complete dissolution. These treated 96-well plates were measured for absorbance with an enzyme label and the absorption wavelength was 577 nm. Finally, the cell survival rate and the half maximal inhibitory concentration (IC_{50}) of compound **A3** on the cells were calculated from the obtained absorbance values.

3. Results and discussion

3.1 Synthesis of new of fluorescent probes

The fluorescent probes **A1-A6** were synthesized by a simple 2-step preparation as shown in Scheme S1. The intermediate **a** (*N*-methyl-4-chloro-2-methylquinoline) was prepared by the methylation of 4-chloro-2-methylquinoline. The followed synthesis via a 3-component reaction using *N*-methyl-4-chloro-2-methylquinoline, a selected amine (morpholine, piperidine, 4-methylpiperidine, pyrrolidine, propylamine, or *N*-butyl amine) and *p*-dimethylaminobenzaldehyde in one-pot gave a series of new fluorescent DNA binding probes. The yields of the compounds were found to be 87.6 - 90.5 %. All the isolated compounds were characterized with ^{1}H NMR, ^{13}C NMR, and high resolution MS (**Figure S1-S6**).

3.2 Spectroscopic properties and properties of the fluorescent probes

The spectral properties of the DNA binding probes **A1-A6** were listed in **Table 1**. The probes exhibit an absorption maximum in the visible region between 421-451 nm (**Figure S7**) and have no fluorescence property in Tris-HCl buffer solution at pH = 7.4. When the probes bind to double-stranded or G4-DNA in the buffer solution, the corresponding wavelengths of absorption maximum were red-shifted. For example, the absorption maxima of the probes bound to pu27 (for excitation) were found shifted to 453-498 nm and the maximum emission wavelengths were in the orange region at 610 nm approximately, which gave a large Stokes shift (112-131 nm). The observation of a large Stokes shift of the probes may indicate that the probes possess good anti-interference effect and less energy loss property [[40]].

Table 1. The spectroscopic properties of the fluorescent probes.[a]

Probe[b]	λ_{Abs} (nm)	λ_{ex} (nm)	λ_{em} (nm)	Stokes shift[c]	Φ_f[d]
A1	451	483	610	127	0.11
A2	442	482	611	129	0.47
A3	443	498	610	112	0.56
A4	421	453	584	131	0.42
A5	422	462	583	121	0.46
A6	422	462	583	121	0.44

[a] Experiments were performed in 10 mM Tris-HCl buffer at pH = 7.4.

[b] The concentration of the probe used is 5.0 µM.

[c] Stokes shift.

[d] Relative fluorescence quantum yield of probes upon addition of 9.0 µM pu27; Standard of the relative fluorescence quantum yield is done with sodium fluorescein (Φ_f = 0.85, in CH_3OH).

Table 2. The molecular binding property of the probes in sensing of pu27 G-quadruplex DNA.[a]

Probe[a]	F/F_0	L_rd (µM)[b]	LOD (nM)[c]	R^2	K ($\times10^6$ M^{-1})[d]
A1	29.87	0.85-2.84	6.76	0.999	1.00
A2	44.56	0.14-1.28	4.23	0.999	1.89
A3	43.61	0.14-1.28	4.01	0.999	1.67
A4	45.71	0.14-1.28	2.04	0.977	2.56
A5	24.40	3.55-6.53	16.38	0.998	0.95
A6	29.96	2.84-5.68	10.65	0.997	1.05

[a] Concentration of the probe used was 5.0 µM, the final concentration of pu27 was 9.0 µM.

[b] Linear concentration range for the detection of pu27.

[c] Limit of detection for pu27.

[d] Equilibrium binding constant (*K*) of the probe with pu27 at 25 °C.

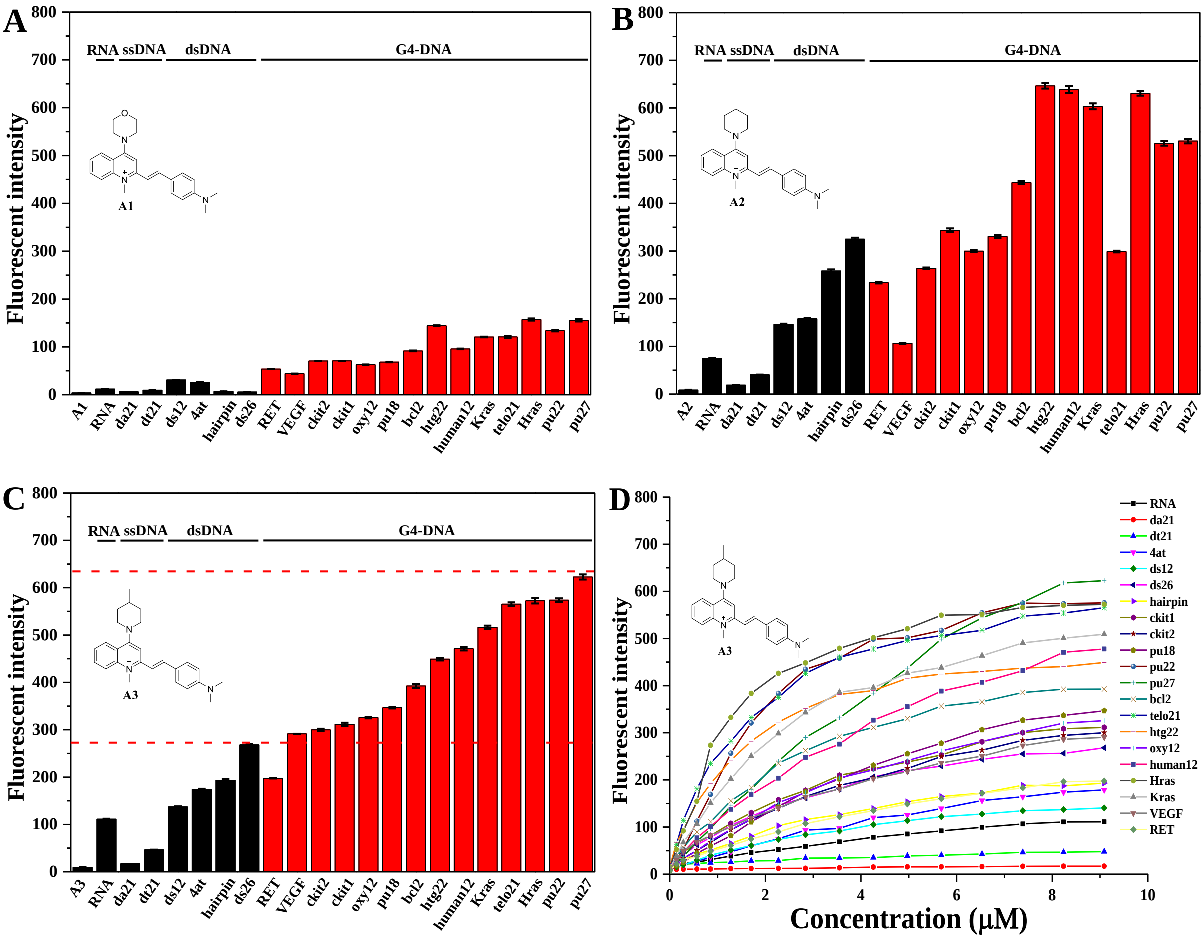

Figure 1. (A-C) Fluorescence screening of the probes **A1-A3** with different DNA and RNA substrates including single-stranded DNA: da21, dt21; duplex DNA: 4at, ds12, ds26, hairpin; G-quadruplex DNA: ckit1, ckit2, pu18, pu22, pu27, bcl2, telo21, htg22, oxy12, human12, Hras, Kras, VEGF and RET. The concentration of the probes was fixed at 5 μM and the nucleic acids was fixed at 9.0 μM in a Tris-HCl buffer containing 60 mM KCl. (D) Fluorescence titration: the enhanced intensity of **A3** (5.0 μM, λ_{ex} = 498 nm, λ_{ex} = 610 nm) with different concentration of nucleic acids at pH 7.4 in Tris-HCl buffer containing 60 mM KCl.

The fluorescence signal changes due to the interaction of the probe and nucleic acids were investigated with fluorescence titrations. From the screening experiments shown in **Figure 1 (A-C)**, probe **A1** only exhibited relative weak fluorescence enhancement upon interacting with various types of nucleic acids (F/F_0 = 1.6-40.7 folds). In general, with respect to the fluorescence response, **A1** showed slightly better selectivity towards G4-DNA than RNA, single-stranded DNA (ssDNA) and double-stranded DNA (dsDNA). The fluorescence response of **A2** seems improved significantly as indicated by their strong induced emission signals upon interaction with the nucleic acids (F/F_0 = 2.2-75.3 folds). Obviously, the replacement of morpholine by piperidine group, which is substituted in the quinolinium ring of **A2**, did not cause the loss of binding selectivity towards G4-DNA and also greatly improved the fluorescence binding signal. In general, in terms of induced emission signal intensity, the signal of G4-**A2** interaction is almost 2 to 4 folds higher than that of G4-**A1** (**Figure 1 A** and **B**). Interestingly, these two probes possess a very similar molecular structure and excitation and emission wavelength. The only difference is the morpholine ring bearing an oxygen atom, which is a very good hydrogen bond acceptor. However, the results indicate that the molecular structure of **A2** may be able to adopt a much better interaction orientation in the G4-binding pockets than **A1** does as the Φ_f was increased from 0.11 to 0.47. It may probably originate from a more efficient suppression of the radiationless deactivation of the excited state in the binding site, which could also be attributed to the effective restriction of the rotation of dimethylaniline moiety connecting to the quinolinium ring through a rotatable ethylene bridge [[41]]. The strength of the interaction could be further indicated by comparing their equilibrium binding constants with pu27 G4-DNA shown in **Table 2**. The binding constant (*K*) for pu27-**A1** was found to be 1 x 10^6 M^{-1}, which is obviously weaker than that of **A2** (1.89 x 10^6 M^{-1}) and **A3** (1.67 x 10^6 M^{-1}) under the same interaction conditions.

Despite **A2** showed merit properties in signaling enhancement for molecular interactions and better binding preference towards G4-DNA substrates over other types of nucleic acids, its molecular structure was further optimized by introducing a 4-methylpiperidine group, which is just slightly bulky than piperidine group, at the 4-position of the quinolinium ring to probe the interaction environments in terms of ligand size and rigidity of the G4-binding pocket. From **Figure 1 C**, the fluorescence screening of various nucleic acids, in general, **A3** has some improvements for the fluorescence signal upon binding with G4s while decrease slightly the interaction signal for the dsDNA substrates (hairpin, ds26), which implies the discrimination of G4s from dsDNA is improved with the 4-methylpiperidine group. It may be due to the methyl increasing the rigidity of the molecule and thus offering a better interaction orientation of the flexible groups of the probe in the G4-binding pocket. When the 4-methylpiperidine group at the quinolinium ring was replaced by a slightly smaller cyclic group, pyrrolidine (**A4**), or a more flexible alkyl chained amine groups, propylamine (**A5)** and *N*-butyl amine **(A6)**, it was found that both **A4, A5**, and **A6** probes exhibited very poor ability in the discrimination of dsDNA and G4-DNA in terms of the observed interaction signal (**Figure S8**). These nucleic acid-ligand interaction results may indicate that the molecular fragments of morpholine, piperidine, pyrrolidine, propylamine and butyl amine are less specific towards the G4-DNA structure.

The fluorescence quantum yield is an important spectral parameter of small molecular fluorescent probes because it indicates the ability of the fluorescent material converting the absorbed light energy into fluorescence, which is one of the most essential factors for sensing applications in materials science. The quantum yields of probes **A1-A6** upon bound to pu27 were investigated and the quantum yields were found to be 0.11-0.56 (**Table 1**). Among the three probes bound to pu27, **A1** offered the lowest quantum yield (Φ_f = 0.10), while A2 (Φ_f = 0.47) and **A3** (Φ_f = 0.56) are found comparable and both are much greater than that **A1**. From the quantum yield results, it may suggest that **A3** with a 4-methylpiperidine substituent could be a good pu27 G4-DNA sensor as it can offer strong fluorescence signal intensity during the molecular interaction dynamic study in aqueous medium under physiological conditions.

3.3 Detection limit and binding affinity of fluorescent probe to G-quadruplex DNA

The ability to determine a specific target of nucleic acids at low concentration is an important indicator of the performance of a fluorescent probe for biosensing. The sensitivity of probes **A1-A6**, in terms of limit of detection (LOD), was examined with fluorescence titration experiments using pu27 as a model substrate. As shown in Table 2, the detection limits of **A1-A6** are 6.6 nM, 4.2 nM, 4.0 nM, 2.0 nM, 16.3 nM and 10.6 nM, respectively. **Figure 2 A** shows the fluorescence titration of probe **A3** and pu27 in a pH = 7.4 Tris HCl (10 mM) buffer solution. With the increase concentration of pu27, the fluorescence intensity of **A3** also increases accordingly and reaches a plateau at 9.0 μM. It was found that the concentration of pu27 in the range of 0.14-1.28 μM showed an excellent linear relationship with respect to the fluorescence signal enhancement of pu27-**A3** interaction (**Figure 2 B** and **C**). The results demonstrated that probe **A3** is able to detect pu27 at sub-μM level with a LOD of 4.0 nM (S/N = 3), which is much better than commercial fluorescent probe thiazole orange (LOD limit = 48.7 nM for pu27) [[42]]. In order to observe the fluorescence stability of the probes after binding to G4-DNA against photo-bleaching, we used pu27 and telo21 to bind to **A3** at a fixed concentration and monitored their fluorescence intensity changes for 3600 s (**Figure 2 D**). The fluorescence stability of **A3** was very robust and the signal intensity representing the DNA-ligand complex was retained higher than 89 % in both cases.

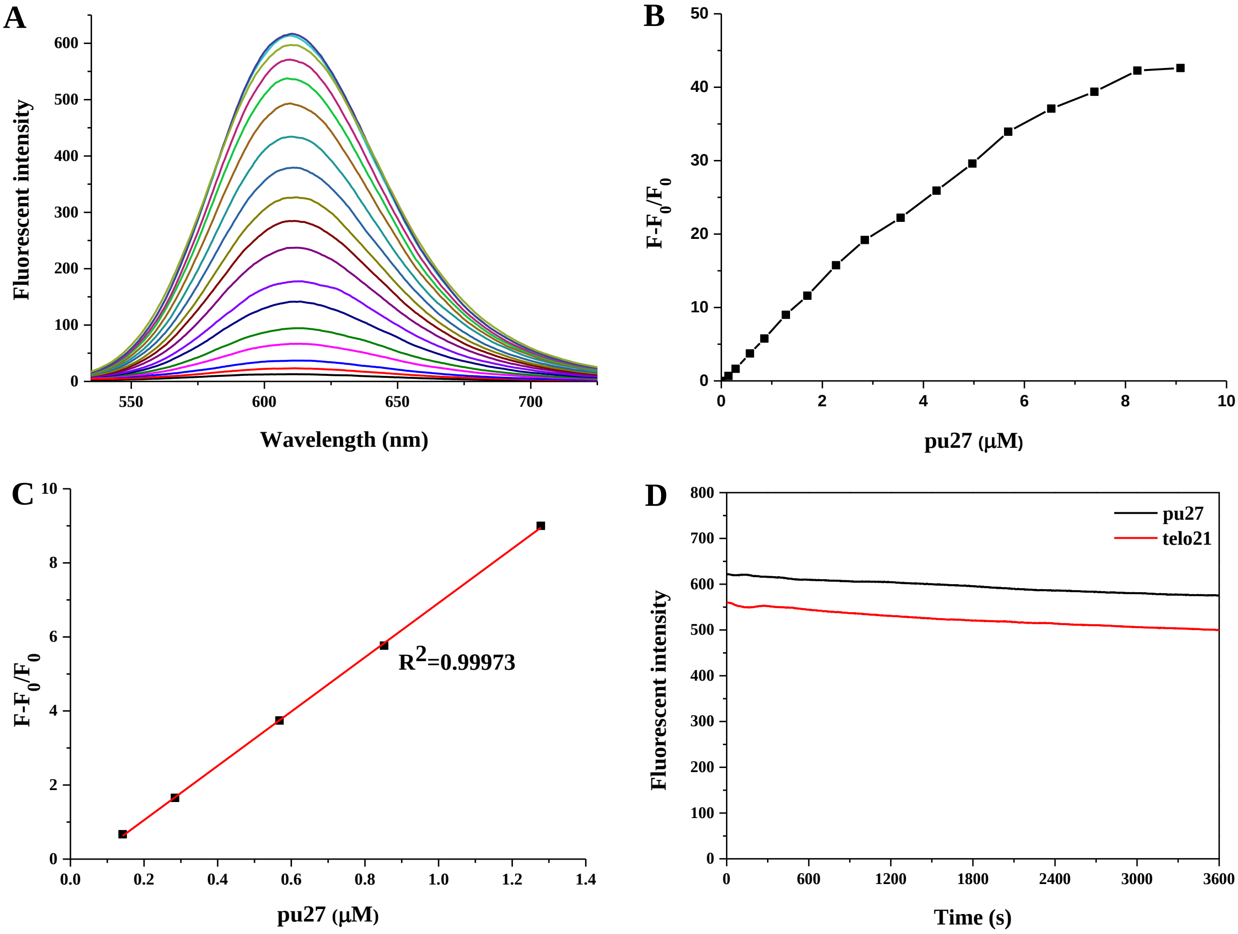

Figure 2. (A) Fluorescence titration spectra of **A3** with pu27 in a Tris-HCl buffer (10 mM, pH 7.4) containing 60 mM KCl. (B) The fluorescence titration of probes **A3** (5 μM) with stepwise addition of G-quadruplex pu27 (0–9.0 μM). F_0 represents the fluorescence intensity without pu27 and F represents the fluorescence intensity after adding pu27. (C) Linear relationship of probe **A3** in the detection of pu27. (D) The curve of fluorescence intensity with time (3600 s) after the combination of probe **A3** with pu27 and telo21 (9.0 μM).

*3.4 Study on the interaction between probe **A3** and nucleic acid by UV-Vis absorption spectroscopy*

UV-Vis absorption analysis is one of the commonly used methods to study the interaction characteristics between nucleic acids and small molecular binding ligands. UV-Vis titration experiments were therefore carried out using **A3** and ssDNA (dt21), dsDNA (ds26), and G-quadruplex DNA (telo21, pu27). From **Figure 3 A**, the broad absorption peaks, at 380 and 443 nm respectively, decreased gradually when increasing the concentration of dt21. For ds26, the intensity of the absorption peaks at 380 and 443 nm decreased and a new and weak absorption peak at 462 nm was formed gradually as increasing the concentration of DNA substrate. When **A3** titrated with G4-DNA, increasing of the concentration of telo21, the intensity of the absorption peaks at 380 and 443 nm decreased and a new and obvious absorption peak at 487 nm was also formed. With the increase concentration of pu27, the absorption peaks at 380 and 443 nm decreased with larger amplitudes and the new absorption peak formed at 498 nm become more remarkable.

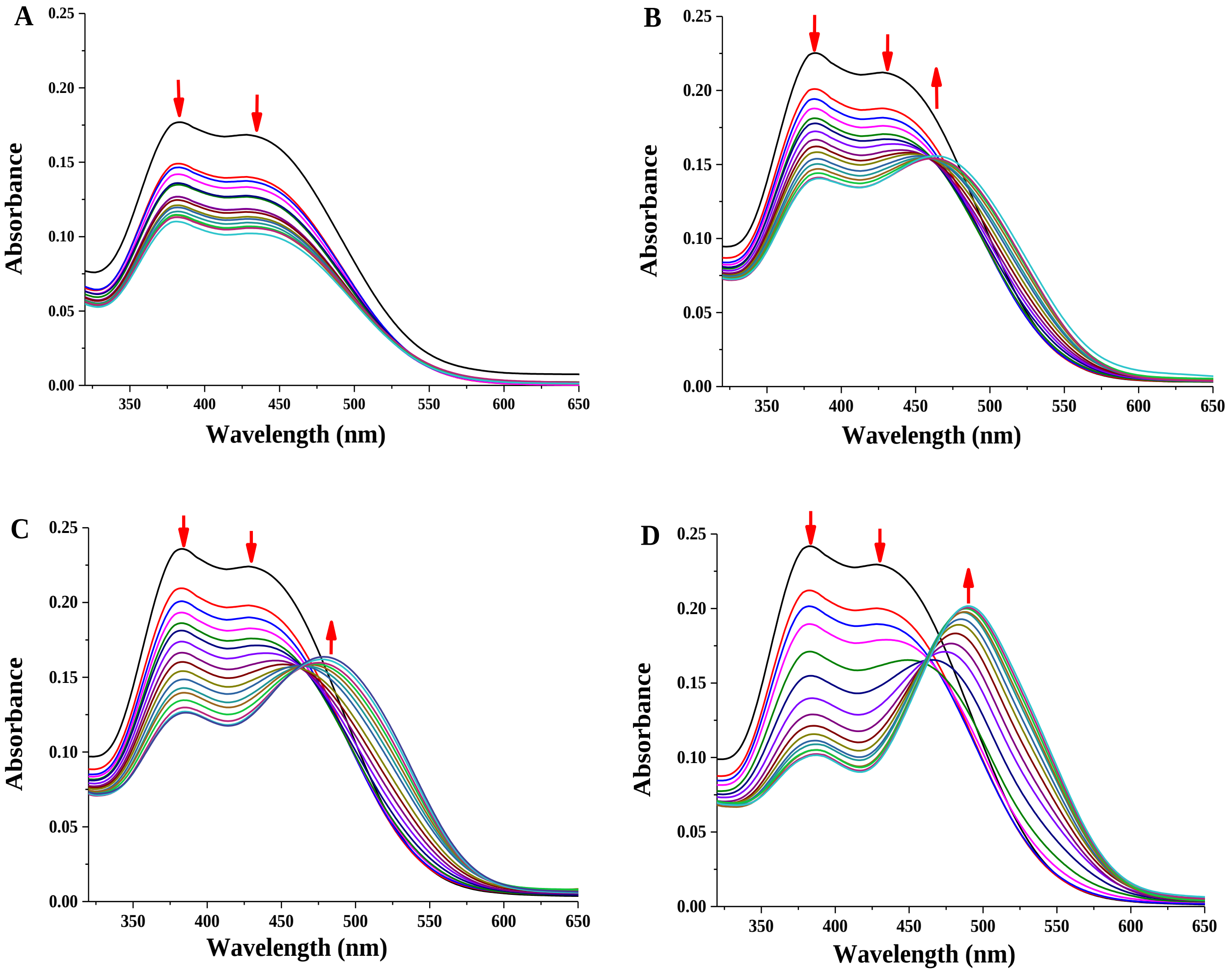

Figure 3. UV-vis titration of **A3** (15 μM) with various DNA (0-9.0 μM) in 10 mM Tris-HCl buffer (60 mM KCl). (A) Single-stranded DNA: dt21; (B) Duplex DNA: ds26; (C) G4-DNA: telo21; (D) G4-DNA: pu27.

By comparing the UV-Vis titrations results, we may infer that the interaction between **A3** and dt21 or ds26 is relatively weak than that of telo21 or pu27, which cause obvious changes in the absorption spectra. The significant new peak formation with G4-DNA substrates may be probably due to the structural change of **A3** upon bound to the binding pocket of G4-DNA. The increase in longer wavelength absorption may be attributed to a more *π*-conjugated system of **A3** developed when interacting with G4-binding pocket. More importantly, there is an isosbestic point appeared for both telo21 and pu27, which probably indicates a multiple interaction mode for the **A3**–G4-DNA complex formation.

*3.5 Study the interaction and conformation between **A3** and G4-DNA with Circular Dichroism*

Some small molecules may cause G4-DNA structural changes and affect its physiological function. Through circular dichroism (CD) measurement, it is possible to observe the change of G-quadruplex structures. We therefore investigated the influence of **A3** on G4-structures of telo21 and pu27 in the presence of K^+ ions [[43]]. From **Figure 4 A**, an intensive positive peak at 290 nm and a negative peak at 235 nm were observed for telo21, which is a characteristic hybrid-quadruplex structure. The addition of **A3** to interact with telo21 or increasing the concentration of **A3** did not change the absorption pattern, meaning that **A3** does not cause conformation change upon interacting with telo21.

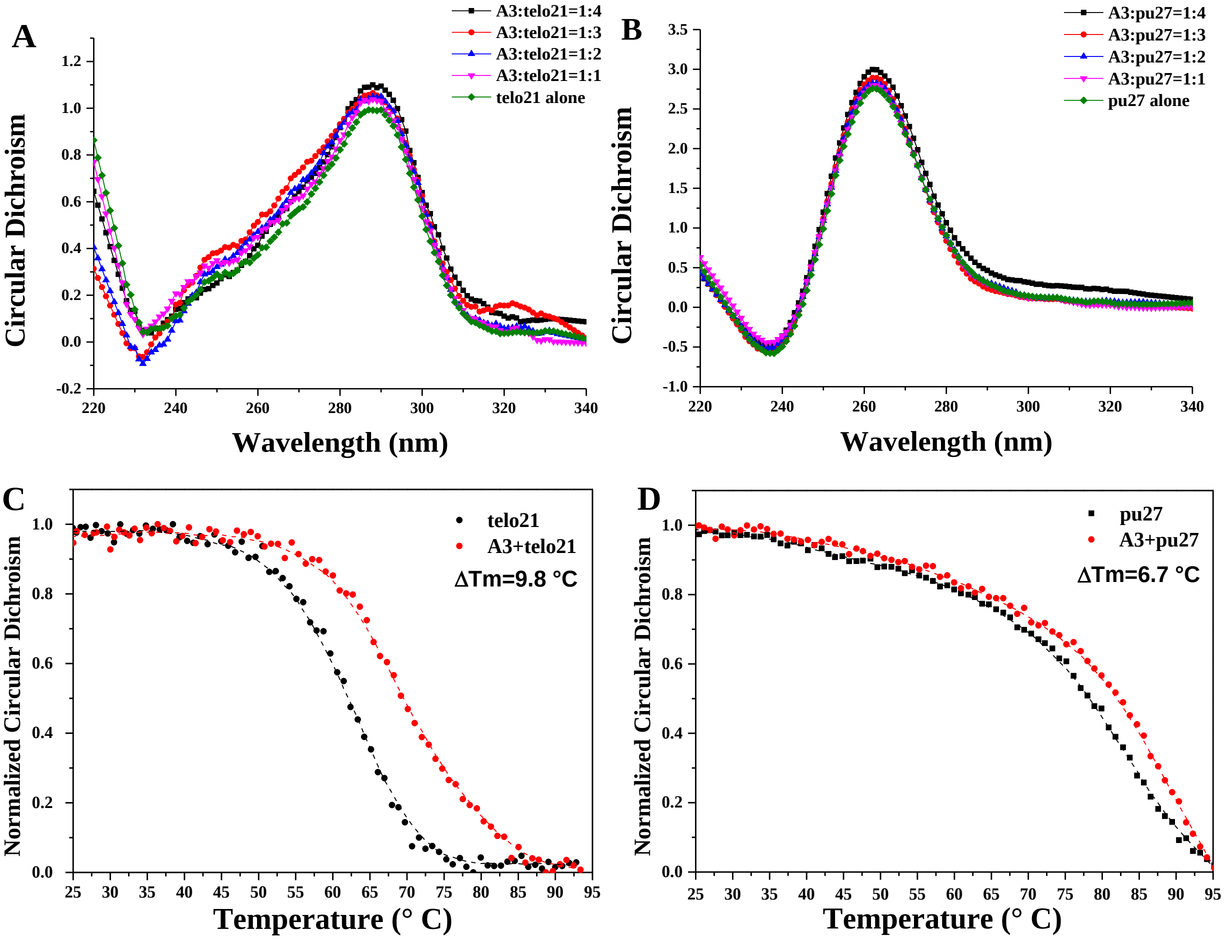

Figure 4. (A) CD spectra of telo21 binding with **A3** in 10 mM Tris-HCl buffer at pH 7.4 with 60 mM KCl. (B) CD spectra of pu27 binding with **A3** in 10 mM Tris-HCl buffer at pH 7.4 with 60 mM KCl. (C) Normalized CD signal of the telo21 G-quadruplex during melting process. The G-quadruplex was characterized by the

positive peak at 290 nm. (D) Normalized CD signal of the pu27 G-quadruplex during melting process. The G-quadruplex was characterized by the positive peak at 265 nm.

In the case of pu27, it showed a distinctive parallel-quadruplex structure, which indicated by a positive peak at 265 nm and a negative peak at 240 nm, respectively (**Figure 4 B**). It was also found that **A3** did not cause structural change upon interaction. The results imply that **A3** may be used as a red fluorescent sensing probe targeting G4-structures for bio-imaging applications without interfere their conformation change.

The stabilization ability of **A3** to G4-structures was also evaluated by the melting point tests. **Figure 4 C** and **D** showed the normalized CD signal profile of **A3**–telo21 and **A3**–pu27 complexes during melting process. It was found that the melting point of telo21 was increased by 9.8 °C and pu27 increased by 6.7 °C upon addition of **A3**, respectively. The increased melting temperature of the complex may suggest that **A3** can stabilize G4-structure.

*3.6 Study the ligand–G4 interactions with NMR titration using **A3** and G4-DNA as a model*

In order to obtain more information on the binding mode of the **A3**–G4-DNA complex in solution, ^{1}H NMR titration experiments were conducted. Since **A3** showed higher binding preference towards promoter G4 and telomere, we therefore selected Htg24 (telomeric G4-DNA) and pu22 (promoter G4-DNA) to investigate and compare their interaction difference. The structures of these two G4-DNA substrates were fully characterized by ^{1}H NMR and the signals of guanine fragments were assigned. As shown in **Figure 5**, the imino protons were well identified between 10-13 ppm and were found consistent with literature reports [[47]]. In **Figure 5 A**, with 1 and 2 equivalents of **A3** added to the free Htg24 G4-DNA solution, we observed a significant proton signal change in chemical shifts for the guanines G3, G22, G23, and a slight change for G10 and G16, which indicates the *in situ* formation of **A3**–Htg24 complex. Their detailed chemical shifts were summarized in **Table 3** for comparison. Among many possible binding modes of **A3**–Htg24, we speculated that **A3** is most likely binding to the groove where G3, G22, and G23 located (**Figure 5 A**, marked in red) because the groove is without the loop structure and thus the blocking effect is possibly reduced. It is therefore beneficial for the interaction of **A3** with Htg24. In addition, the chemical shifts of G10 and G16 were found changed slightly, so **A3** may also be interacted with the groove where G10 and G16 located (**Figure 5 A**, marked in green). However, there is a loop formed by three bases under the groove. The motion of the loop may induce a hindrance for **A3** to establish a stable binding with the groove. This interaction mode is therefore less favorable compared to the previous one.

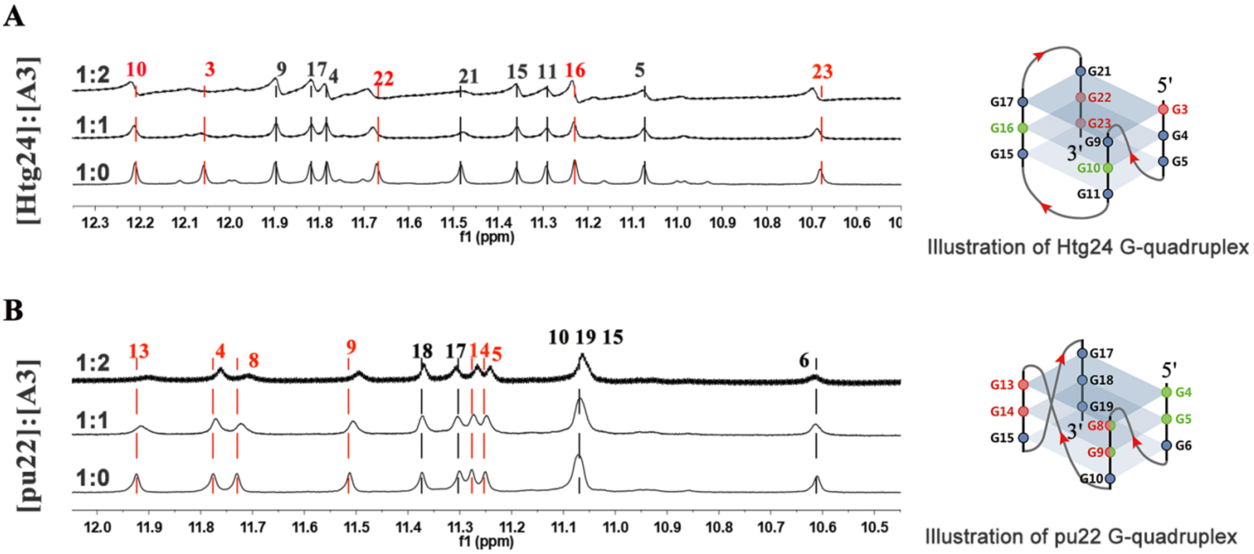

Figure 5. Chemical shift perturbation analysis of G-quadruplexes with **A3**. (A) Imino proton regions of the ^{1}H NMR spectra of Htg24 either alone (bottom) or with **A3** at a ratio of 1:1 (middle) and 1:2 (top). (B) Imino proton regions of the ^{1}H NMR spectra of pu22 either alone (bottom) or with **A3** at a ratio of 1:1 (middle) and 1:2 (top). The assays were performed in 25 mM KH_2PO_4 buffer (70 mM KCl, 10% D_2O, pH 7.4) using 600 MHz Bruker spectrometers at 25 °C, and the final concentration of G4-DNA was 300 μM.

For **A3**–pu22 interactions, as shown in **Figure 5 B**, when adding 1 and 2 equivalents of **A3** to the free pu22 solution, the chemical shifts for the imino protons including G13, G8, G9, G14, G4 and G5 changed obviously, which indicated that the interaction of **A3** and pu22 G4-DNA may have two possible modes. The first one could be **A3** interacted with the groove where G13, G8, G9 and G14 located (**Figure 5 B**, marked in red) and the second possibility seems to be the interaction of **A3** with the groove where G8, G9, G4 and G5 located (**Figure 5 B**, marked in green). Interestingly, in these six groups of imino protons, the chemical shift changes of G13, G8, G9, and G14 are larger than G4 and G5 (**Table 4**), which may imply that the first binding mode proposed is more favorable than the second one. We attempted to find out what factors may cause such difference from the structure of pu22 G4-DNA and we speculated that it is possibly arising from the loop structure. The loop structure formed in the groove where G13, G14, G8, and G9 located is formed by two bases, while the loop structure formed in the groove where G8, G9, G4, and G5 located is just formed by one base. In the case where both have a loop structure, the longer the loop structure, the larger the pockets may be formed. The large pockets could be more favorable for the small-sized binding probe to enter the groove. Therefore, in the interaction mode of **A3**–pu22 could be favorable to bind to the groove where G8, G9, G13 and G14 located.

Table 3. Chemical shift of imino proton of Htg24 alone or after addition of ligand **A3** from NMR spectra.

A3:Htg24	G3	G22	G23	G10	G16
0:1	12.057	11.671	10.682	12.210	11.229
1:1	12.062	11.677	10.687	12.211	11.230
2:1	12.088	11.687	10.695	12.219	11.233
Δ chemical shift	0.031	0.016	0.013	0.009	0.004

Table 4. Chemical shift of imino proton of pu22 alone or after addition of ligand **A3** from NMR spectra.

A3:pu22	G13	G8	G9	G14	G4	G5
0:1	11.924	11.730	11.512	11.277	11.776	11.251
1:1	11.916	11.721	11.506	11.273	11.767	11.245
2:1	11.899	11.708	11.493	11.264	11.764	11.241
Δ chemical shift	-0.025	-0.022	-0.019	-0.013	-0.012	-0.010

*3.7 The application of **A3** in visualization of G-quadruplex DNA in vitro and in vivo*

To explore the potential applications of **A3** in nucleic acid staining and live cell imaging, we demonstrated the use of **A3** to stain G4-DNA substrates in solution, PAGE and in live PC3 cells. As shown in **Figure 6**, **A3** at 5 μM is able to visualize a number of G4-DNA including bcl2, pu27, htg22, telo21, Kras in Tris-HCl buffer solution under UV light illumination. The dsDNA ds26 was also found weakly stained while dt21 and 4at did not induce fluorescence, which indicated that **A3** is more suitable for fluorescence visualization of G4-DNA substrates. In addition, as shown in **Figure 7**, **A3** can selectively stain bcl2, pu27, htg22, telo21, and Kras in polyacrylamide gel electrophoresis (PAGE) while dt21, ds26 and 4at only generated very weak or even no staining signal. Compared to the commercial dye, SYBR Gold, **A3** is much more selective towards G4-DNA substrates.

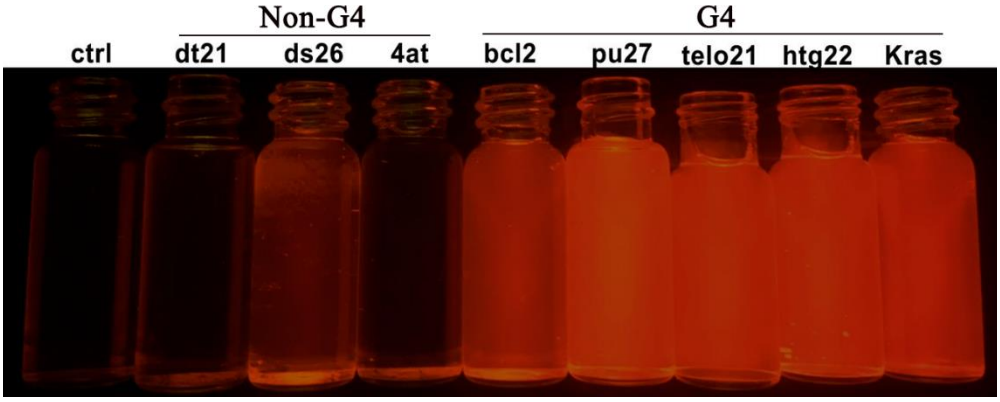

Figure 6. The fluorescent signal response of **A3** under a laboratory UV-chamber (illuminated at 302 nm) upon addition of nucleic acids (5.0 μM): dt21, ds26, 4at, bcl2, pu27, telo21, htg22, Kras. The concentration of **A3** was 5 μM in a Tris-HCl buffer containing 60 mM KCl, and the incubation time was 10 min.

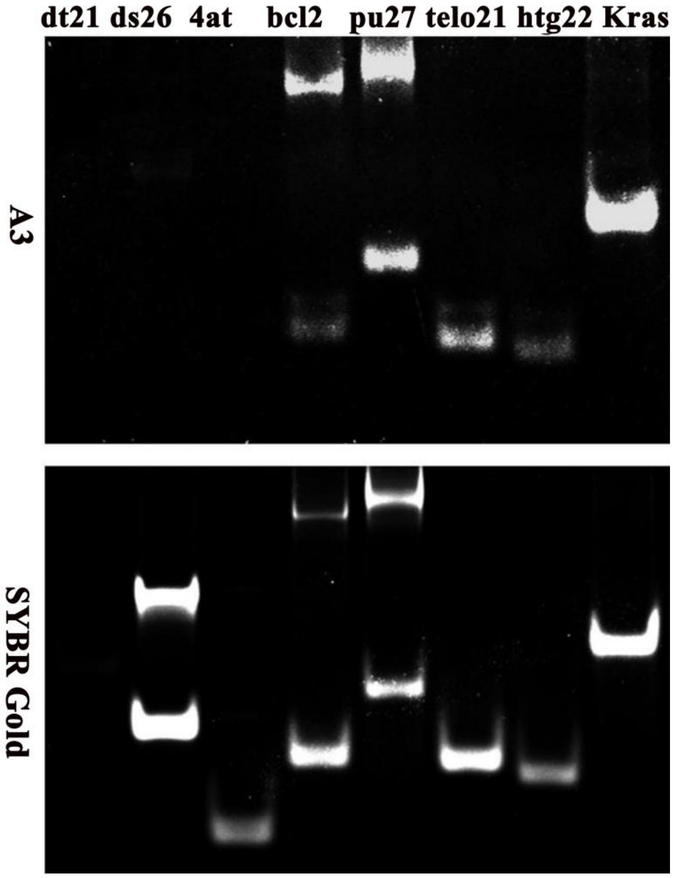

Figure 7. Gel electrophoresis (20 % acrylamide in 1 × TBE) of dt21, ds26, 4at, bcl2, pu27, telo21, htg22, Kras at a concentration of 5.0 μM and was stained with **A3** (5.0 μM) for 30 min.

It is well-known that the G-rich genes are concentrated in the nucleus, especially in the nucleolus region. We therefore used confocal microscopy to study the bio-imaging performance of **A3** in live PC3 cells. From **Figure 8**, the PC3 cell after treated with **A3** showed intensive fluorescence signal in the nucleolus region and some thinly dispersed foci in the cytoplasm. However, the non-selective DAPI dye brightening up the whole nucleus but the nucleolus. The merged image gives clearly the locations of the cell stained with **A3**, where may have G4-DNA present. To further confirm **A3** binds to DNA rather than RNA in cells, we used DNA enzyme or RNA enzyme to treat the fixed PC3 cells before staining. From **Figure 9**, after RNase treatment, the cell images were almost unchanged and strong fluorescence signals remained in the nucleolus region. On the contrary, the PC3 cells were treated with DNase, almost all of the fluorescence signals disappeared. The results suggest that **A3** primarily binds to DNA rather than RNA *in vivo*. In addition, in an attempt to prove that the site of **A3** in the cell is G-quadruplex DNA, a specific G-quadruplex antibody BG4 was used to show the co-localization with **A3** in the immunofluorescence experiments. As shown in **Figure 10**, the **A3** foci and BG4 staining co-localized well in PC3 cells, which indicated that both **A3** and BG may have the same cellular targets. The result further confirmed that **A3** can preferentially bind to G4-DNA in live cells and thus the real-time fluorescence visualization of G4-DNA structures *in vivo* is realized.

To evaluate of the fluorescence performance of **A3** in biosensing targeting G4-DNA biomolecules, we summarized the recently reported fluorescence probes and listed in **Table S3** form comparison. Eight factors including substrate selectivity, excitation wavelength, emission wavelength, Stokes shift, F/F_0, binding specificity, the limit of detection and in cellulo imaging, were selected as the parameters for a comprehensive comparison of the merits of sensing probes using for biosensing and bioanalytical purposes. From the summary, we found that **A3**, comparing with other probes targeting G4-DNA substrates, has a larger Stokes shift, lower detection limit (down to 4 nM) and stronger G4 binding ability (16.67×10^5 M^{-1}). These factors render our red fluorescent binding probe is a good biosensor or imaging agent for both *in vitro* and *in vivo* applications targeting G4-DNA. Furthermore, cytotoxicity assays demonstrated that the probe has very low cytotoxicity against both PC3 cancer cells and 16HBE normal cells (**Figure S16**).

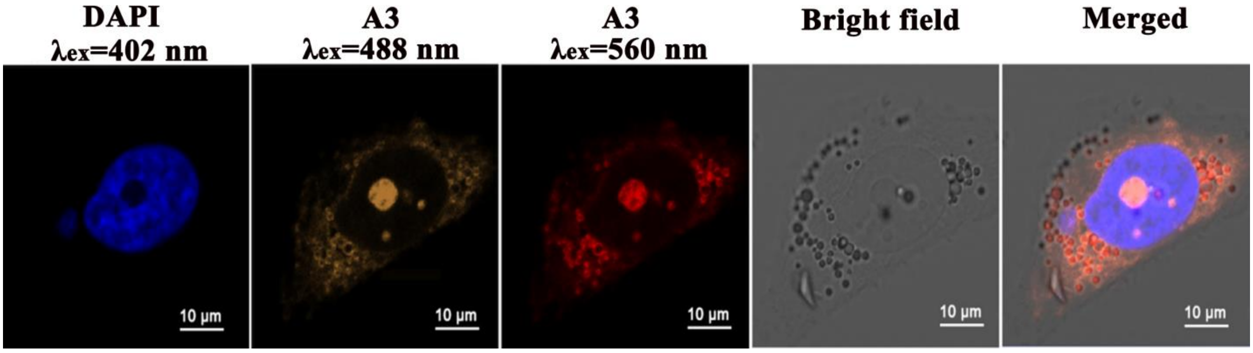

Figure 8. Fluorescence images of live PC3 cells stained with 5 μM **A3** for 30 min and 1.0 μM DAPI for 10 min. The 630x magnification in all figures. Scale bar is 10 μm.

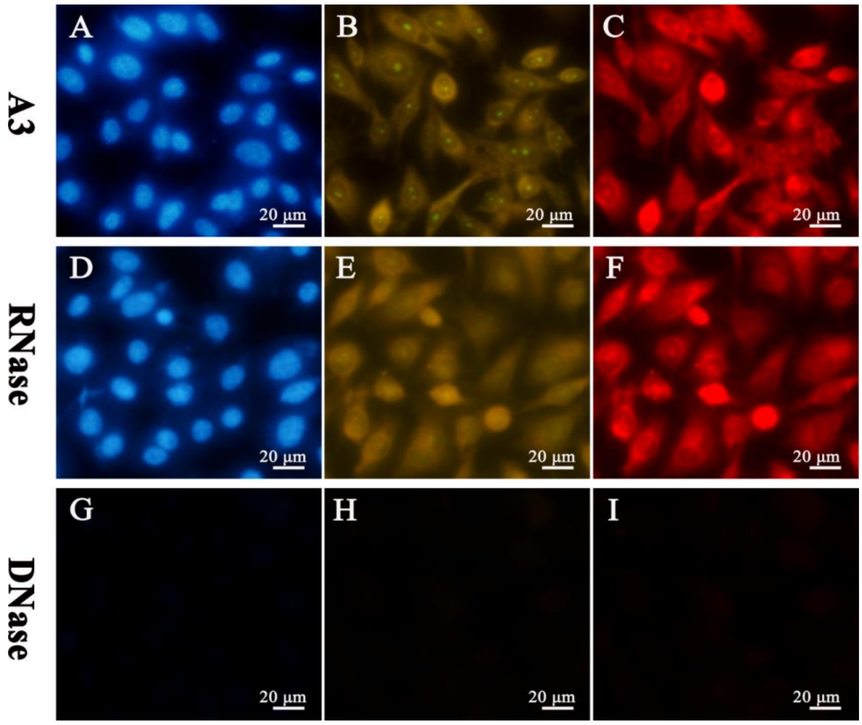

Figure 9. (A) 1.0 μM DAPI for 10 min; (B) and (C) Fluorescence images of live PC3 cells stained with 5 μM **A3** for 30 min; (D) 1.0 μM DAPI for 10 min and RNase treated for 30 min; (E) and (F) Fluorescence images of live PC3 cells stained with 5 μM **A3** for 30 min and RNase treated for 30 min; (G) 1.0 μM DAPI for 10 min and DNase treated for 30 min; (H) and (I) Fluorescence images of live PC3 cells stained with 5 μM **A3** for 30 min and DNase treated for 30 min.

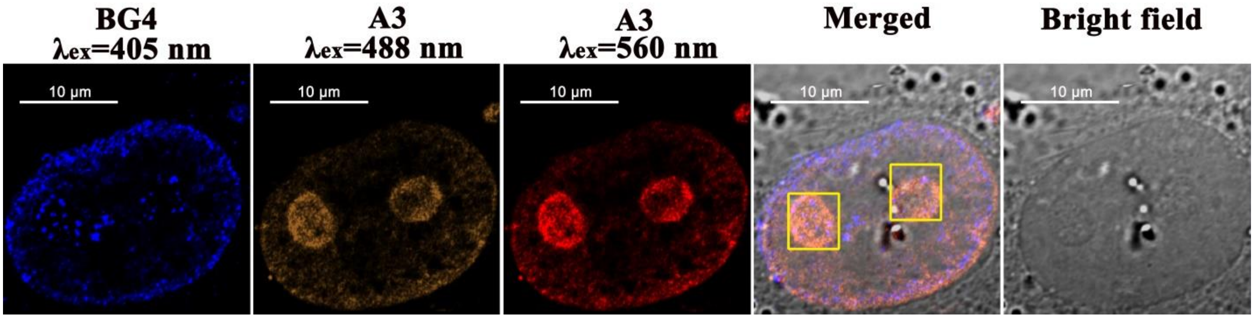

Figure 10. Images of immunofluorescence analysis using **A3** and BG4 antibody in PC3 cell.

4. Conclusion

In conclusion, a new and red fluorescent probe showing large Stokes shift, high fluorescence quantum yield, robust against photo-bleaching and high selectivity towards G4-DNA biomolecules with strong binding affinity was developed. The probe was found exhibited much stronger fluorescence enhancement upon bound to pu27 than the non-G4-DNA *in vitro*. An excellent linear relationship with respect to the induced fluorescence signal due to pu27-porbe interaction was observed with a LOD of 4.0 nM in pu27 detection. The probe is also able to realize fluorescence visualization in aqueous solution, PAGE staining and live cell imaging. In addition, in the immunofluorescence analysis using the probe and BG4 antibody, the **A3** foci and BG4 staining were co-localized well in PC3 cells. The results confirm that the new probe can selectively bind to G4-DNA in live cells and then realize the fluorescence visualization of G4-DNA structure.

Acknowledgment

This work was supported by the National Nature Science Foundation of China (81473082), Nature Science Foundation of Guangdong Province, China (Grant No.: 2017A030313078, 2017A030313071, and 2019A1515011799). The authors are also grateful to the support from the Department of Agriculture and Rural Affairs of Guangdong Province, China (2018LM2175).

Reference

[1] S. Zimmermann, U. M. Martens, Telomeres and telomerase as targets for cancer therapy, Cell. Mol. Life. Sci. 64 (2007) 906 - 921.

[2] J. L. Huppert, B. Shankar, Prevalence of quadruplexes in the human genome, Nucleic Acids Res. 33 (2005) 2908 - 2916.

[3] K. V. Prasanth, D. L. Spector, Eukaryotic regulatory RNAs: an answer to the ‘genome complexity’ conundrum, Gene. Dev. 21 (2007) 11 - 42.

[4] B. Tian, P. C. Bevilacqua, A. Diegelman-Parente, M. B. Mathews, The double-stranded-RNA-binding motif: interference and much more, Nat. Rev. Mol. Cell Bio. 5 (2004) 1013 - 1023.

[5] N. Saini, Y. Zhang, K. Usdin, K. S. Lobachev, When secondary comes first - The importance of non-canonical DNA structures, Biochimie 95 (2013) 117 - 123.

[6] T. A. Brooks, S. Kendrick, L. Hurley, Making sense of G-quadruplex and i-motif functions in oncogene promoters, FEBS J. 277 (2010) 3459 - 3469.

[7] K. Jaroslav, I. Kejnovská, D. Renčiuk, M. Vorlíčková, Circular dichroism and conformational polymorphism of DNA, Nucleic Acids Res. 37 (2009) 1713 - 1725.

[8] M. Gellert, M. N. Lipsett, D. R. Davies, Helix formation by guanylic acid, Proc. Natl. Acad. Sci. USA. 48 (1962) 2013 - 2018.

[9] B. Sarah, G. N. Parkinson, H. Pascale, A. K. Todd, N. Stephen, Quadruplex DNA: sequence, topology and structure, Nucleic Acids Res. 34 (2006) 5402 - 5415.

[10] P. Murat, S. Balasubramanian, Existence and consequences of G-quadruplex structures in DNA, Curr. Opin. Genet. Dev. 25 (2014) 22 - 29.

[11] Y. Xu, Chemistry in human telomere biology: structure, function and targeting of telomere DNA/RNA, Chem. Soc. Rev. 40 (2011) 2719 - 2740.

[12] M. L. Bochman, K. Paeschke, V. A. Zakian, DNA secondary structures: stability and function of G-quadruplex structures, Nat. Rev. Genet. 13 (2012) 770 - 780.

[13] Y. Du, X. Zhou, Targeting Non-B-Form DNA in Living Cells, Chem. Rec. 13 (2013) 371 - 384.

[14] E. Johanna, M. Nancy, Gene function correlates with potential for G4 DNA formation in the human genome, Nucleic Acids Res. 34 (2006) 3887 - 3896.

[15] R. Hänsel-Hertsch, M. D. Antonio, S. Balasubramanian, DNA G-quadruplexes in the human genome: detection, functions and therapeutic potential, Nat. Rev. Mol. Cell Bio. 18 (2017) 279 - 284.

[16] R. Daniela, H. J. Lipps, G-quadruplexes and their regulatory roles in biology, Nucleic Acids Res. 43 (2015) 8627 - 8637.

[17] H. J. Lipps, D. Rhodes, G-quadruplex structures: in vivo evidence and function, Trends Cell Biol. 19 (2009) 414 - 422.

[18] S. Neidle, Quadruplex Nucleic Acids as Novel Therapeutic Targets, J. Med. Chem. 59 (2016) 5987 - 6011.

[19] T. Terai, T. Nagano, Small-molecule fluorophores and fluorescent probes for bioimaging, Pflug. Arch. Eur. J. Phy. 465 (2013) 347 - 359.

[20] Y. F. Zhao, C. Chang, P. P. Gai, L. Han, F. Li, B. Li, One-step synthesis of fluorescent organic nanoparticles: The application to label-free ratiometric fluorescent pH sensor, Sens. Actuators B. 273 (2018) 1479 - 1486.

[21] X. Z. Wang, L. Ge, Y. F. Yu, S. S. Dong, F. Li, Highly sensitive electrogenerated chemiluminescence biosensor based on hybridization chain reaction and amplification of gold nanoparticles for DNA detection, Sens. Actuators B. 220 (2015) 942 - 948.

[22] M. Zuffo, A. Guédin, E. D. Leriche, F. Doria, V. Pirota, V. Gabelica, J. L. Mergny, M. Freccero, More is not always better: finding the right trade-off between affinity and selectivity of a g-quadruplex ligand, Nucleic Acids Res. 46 (2018) e115.

[23] X. Y. Luo, B. B. Xue, G. F. Feng, J. H. Zhang, B. Lin, P. Zeng, H. Y. Li, H. B. Yi, X. L. Zhang, H. Z. Zhu, Z. Nie, Lighting up the Native Viral RNA Genome with a Fluorogenic Probe for the Live-Cell Visualization of Virus Infection, J. Am. Chem. Soc. 141 (2019) 5182 - 5191.

[24] R. Kumar, K. Chand, S. Bhowmik, R. N. Das, S. Bhattacharjee, M. Hedenström, E. Chorell, Subtle structural alterations in G-quadruplex DNA regulate site specificity of fluorescence light-up probes, Nucleic Acids Res. 48 (2020) 1108 - 1119.

[25] J. Mohanty, N. Barooah, V. Dhamodharan, S. Harikrishna, P. I. Pradeepkumar, A. C. Bhasikuttan, Thioflavin T as an Efficient Inducer and Selective Fluorescent Sensor for the Human Telomeric G-Quadruplex DNA, J. Am. Chem. Soc. 135 (2013) 367 - 376.

[26] M. Zuffo, S. Ladame, F. Doria, M. Freccero, Tuneable coumarin-NDI dyads as G-quadruplex specific light-up probes, Sens. Actuators B 245 (2017) 780 - 788.

[27] P. Yang, A. D. Cian, M. P. Teulade-Fichou, J. L. Mergny, D. Monchaud, Engineering Bisquinolinium/Thiazole Orange Conjugates for Fluorescent Sensing of G-Quadruplex DNA, Angew. Chem. Int. Edit. 48 (2009) 2188 - 2191.

[28] M. Q. Wang, Y. Wu, Z. Y. Wang, Q. Y. Chen, F. Y. Xiao, Y. C. Jiang, A. Sang, G-quadruplex DNA fluorescence sensing by a bis-amine-substituted styrylquinolinium dye, Dyes Pigments 145 (2017) 1 - 6.

[29] Y. J. Lu, X. L. Guo, M. H. Xu, W. W. Chen, W. L. Wong, K. Zhang, C. F. Chow, Selective visualization of DNA G-quadruplex structures in live cells with 1-methylquinolinium-based molecular probes: The importance of indolyl moiety position towards specificity, Dyes Pigments 143 (2017) 331 - 341.

[30] M. H. Hu, S. B. Chen, Y. Q. Wang, Y. M. Zeng, T. M. Ou, D. Li, L. Q. Gu, Z. S. Huang, J. H. Tan, Accurate high-throughput identification of parallel G-quadruplex topology by a new tetraaryl-substituted imidazole, Biosens. Bioelectron. 83 (2016) 77 - 84.

[31] Q. Li, Y. Kim, J. Namm, A. Kulkarni, G. R. Rosania, Y. H. Ahn, Y. T. Chang, RNA-Selective, Live Cell Imaging Probes for Studying Nuclear Structure and Function, Chem. Biol. 13 (2006) 615 - 623.

[32] C. Wang, Y. J. Lu, S. Y. Cai, W. Long, Y. Y. Zheng, J. W. Lin, Y. Yan, X. H. Huang, W. L. Wong, K. Zhang, C. F. Chow, Advancing small ligands targeting RNA for better binding affinity and specificity: A study of structural influence through molecular design approach, Sens. Actuators B 262 (2018) 386 - 394.

[33] R. S. Tuma, M. P. Beaudet, X. Jin, L. J. Jones, C. Y. Cheung, S. Yue, V. L. Singer, Characterization of SYBR Gold Nucleic Acid Gel Stain: A Dye Optimized for Use with 300-nm Ultraviolet Transilluminators, Anal. Biochem. 268 (1999) 278 - 288.

[34] J. Kapuscinski, DAPI: a DNA-Specific Fluorescent Probe, Biotech. Histochem. 70 (2009) 220 - 233.

[35] G. Song, Y. Sun, Y. Liu, X. Wang, M. Chen, F. Miao, W. Zhang, X. Yu, J. Jin, Low molecular weight fluorescent probes with good photostability for imaging RNA-rich nucleolus and RNA in cytoplasm in living cells, Biomaterials 35 (2014) 2103 - 2112.

[36] G. Biffi, D. Tannahill, J. Mccafferty, S. Balasubramanian, Quantitative visualization of DNA G-quadruplex structures in human cells, Nat. Chem. 5 (2013) 182 - 186.

[37] G. Biffi, D. Tannahill, J. Miller, W. J. Howat, S. Balasubramanian, Elevated Levels of G-Quadruplex Formation in Human Stomach and Liver Cancer Tissues, Plos One 9 (2014) e102711.

[38] H. Y. Liu, Q. Zhao, T. P. Zhang, Y. Wu, Y. X. Xiong, S. K. Wang, Y. L. Ge, J. H. He, P. Lv, T. M. Ou, J. H. Tan, D. Li, L. Q. Gu, J. Ren, Y. Zhao, Z. S. Huang, Conformation Selective Antibody Enables Genome Profiling and Leads to Discovery of Parallel G-Quadruplex in Human Telomeres, Cell Chem. Biol. 23 (2016) 1261 - 1270.

[39] S. G. Zhang, H. X. Sun, L. X. Wang, Y. Liu, H. B. Chen, Q. Li, A. J. Guan, M. R. Liu, Y. L. Tang, Real-time monitoring of DNA G-quadruplexes in living cells with a small-molecule fluorescent probe, Nucleic Acids Res. 46 (2018) 7522 - 7532.

[40] T. Kogure, H. Kawano, Y. Abe, A. Miyawaki, Fluorescence imaging using a fluorescent protein with a large Stokes shift, Methods 45 (2008) 223 - 226.

[41] N. Sun, C. Wang, M. H. Xu, Y. J. Lu, Y. Y. Zheng, Y. Yan, X. L. Xiao, J. Q. Hou, K. Zhang, L. G. Luyt, W. L. Wong, C. F. Chow, The interaction of a structural flexible small molecule with nucleic acid structures: Investigation of the origin of fluorescence signal discrimination in sensing and the utilization in live cell imaging, Sens. Actuators B 250 (2017) 543 - 551.

[42] W. Long, Y. J. Lu, K. Zhang, X. H. Huang, J. Q. Hou, S. Y. Cai, Y. Li, X. Du, L. G. Luyt, W. L. Wong, C. F. Chow, Boosting the turn-on fluorescent signaling ability of thiazole orange dyes: The effectiveness of structural modification site and its unusual interaction behavior with nucleic acids, Dyes Pigments 159 (2018) 449 - 456.

[43] C. V. Dang, MYC on the Path to Cancer, Cell 149 (2012) 22 - 35.

[44] W. C. Hahn, C. M. Counter, A. S. Lundberg, R. L. Beijersbergen, M. W. Brooks, R. A. Weinberg, Creation of human tumour cells with defined genetic elements, Nature 400 (1999) 464 - 468.

[45] S. Neidle, Human telomeric G-quadruplex: The current status of telomeric G-quadruplexes as therapeutic targets in human cancer, FEBS J. 277 (2010) 1118 - 1125.

[46] K. Natalay, L. Hee-Sheung, C. Mar, L. Mikhail, P. Emma, J. H. Kim, M. Oshimura, H. Masumoto, M. P. Teulade-Fichou, Y. Pommier, W. C. Earnshaw, V. Larionov, N. Kouprina, Systematic Analysis of Compounds Specifically Targeting Telomeres and Telomerase for Clinical Implications in Cancer Therapy, Cancer Res. 78 (2018) 6282 - 6296.

[47] K. Kondo, T. Mashima, T. Oyoshi, R. Yagi, R. Kurokawa, N. Kobayashi, T. Nagata, M. Katahira, Plastic roles of phenylalanine and tyrosine residues of TLS/FUS in complex formation with the G-quadruplexes of telomeric DNA and TERRA, Sci. Rep. 8 (2018) 2864.

[48] J. Dai, M. Carver, L. H. Hurley, D. Yang, Solution Structure of a 2:1 Quindoline-c-MYC G-Quadruplex: Insights into G-Quadruplex-Interactive Small Molecule Drug Design, J. Am. Chem. Soc. 133 (2011) 17673 - 17680.

[49] K. N. Luu, T. P. Anh, V. Kuryavyi, L. Lacroix, D. J. Patel, Structure of the Human Telomere in K^+ Solution: An Intramolecular (3 + 1) G-Quadruplex Scaffold, J. Am. Chem. Soc. 128 (2006) 9963 - 9970.

[50] Z. L. Huang, J. Dai, W. H. Luo, X. G. Wang, J. H. Tan, S. B. Chen, Z. S. Huang, Identification of G-Quadruplex-Binding Protein from the Exploration of RGG Motif/G-Quadruplex Interactions, J. Am. Chem. Soc. 140 (2018) 17945 - 17955.

[51] Q. Q. Zhai, C. Gao, J. Q. Ding, Y. S. Zhang, B. Islam, W. X. Lan, H. T. Hou, H. Deng, J. Li, Z. Hu, H. I. Mohamed, S. Z. Xu, C. Y. Cao, S. M. Haider, D. G. Wei, Selective recognition of c-MYC Pu22 G-quadruplex by a fluorescent probe, Nucleic Acids Res. 47 (2019) 2190 - 2204.

[52] M. H. Hu, X. Chen, J. H. Tan, Development of a multitasking fluorescent probe for differentiating G-quadruplex structures, Dyes Pigments. 170 (2019) 107560.

[53] M. H. Hu, J. W. Zhou, W. H. Luo, S. B. Chen, Z. H. Huang, R. B. Wu, J. H. Tan, Development of a smart fluorescent sensor that specifically recognizes the c-MYC G-quadruplex, Anal. Chem. 91 (2019) 2480 - 2487.

[54] M. H. Wang, Y. Zhang, X. Y. Zeng, H. Yang, R. Y. Fu, H. J. Li, A benzo(f)quinolinium fused chromophore-based fluorescent probe for selective detection of c-myc G-quadruplex DNA with a red emission and a large Stocks shift, Dyes Pigments. 168 (2019) 334 - 340.

[55] L. L. Li, H. R. Xu, K. Li, Q. Yang, S. L. Pan, X. Q. Yu, Mitochondrial G-quadruplex targeting probe with near-infrared fluorescence emission, Sens. Actuators B. 286 (2019) 575 - 582.

[56] M. Q. Wang, J. Xu, L. Zhang, Y. Liao, H. Wei, Y. Y. Yin, Q. Liu, Y. Zhang, , Tuning the selectivity of N-alkylated styrylquinolinium dyes for sensing of G-quadruplex DNA, Bioorg. Med. Chem. 27 (2019) 552 - 559.

[57] F. L. Gao, S. H. Cao, W. Sun, S. Long, J. L. Fan, X. J. Peng, Development of a two-photon carbazole derivative probe for fluorescent visualization of G-quadruplex DNA in cells, Dyes Pigments. 171 (2019) 107749.

[58] Y. Q. Wang, M. H. Hu, R. J. Guo, S. B. Chen, Z. S. Huang, J. H. Tan, Tuning the selectivity of a commercial cyanine nucleic acid dye for preferential sensing of hybrid telomeric G-quadruplex DNA, Sens. Actuators B. 266 (2018) 187 - 194.

Rational Design of Red Fluorescent and Selective G-quadruplex DNA Sensing Probes: The Study of Interaction Signaling and the Molecular Structural Relationship Achieving High Specificity

Bo-Xin Zheng,[a] Wei Long,[a] Yi-Han Zhang,[a] Xuan-He Huang,[a] Cui-Cui Chen,[a]
Dong-Xiao Zhong,[a] Meng-Ting She,[a] Ze-Xin Chen,[a] Dong-Peng Cai,[a] Yu-Jing Lu,*[,a] and
Wing-Leung Wong*[,b]

[a] School of Biomedical and Pharmaceutical Sciences, Guangdong University of Technology, Guangzhou 510006, P. R. China.
[b] The State Key Laboratory of Chemical Biology and Drug Discovery, Department of Applied Biology and Chemical Technology, The Hong Kong Polytechnic University, Hung Hom, Kowloon, Hong Kong, China.

* Corresponding author
E-mail: luyj@gdut.edu.cn;
E-mail: wing.leung.wong@polyu.edu.hk

List of content

Figure S13 Fluorescence titration spectra of probes **A1-A6** with different concentrations of DNA substrates.

Figure S14 UV-vis titration spectra of probes **A1-A6** with different concentrations of DNA substrates.

Figure S15 The linear fitting of the absorption intensity by the fluorescence emission spectral integral area of the probes **A1-A6** and fluorescein sodium in pu27.

Figure S16 Cells survival viability of PC3 cells and 16HBE cells in probe **A3**.

Table S3 The comparison of red fluorescent probe **A3** with the recently reported analytical systems targeting G4-DNA substrates.

3. Reference

1. Experimental Section

1.1. Synthesis and Characterization

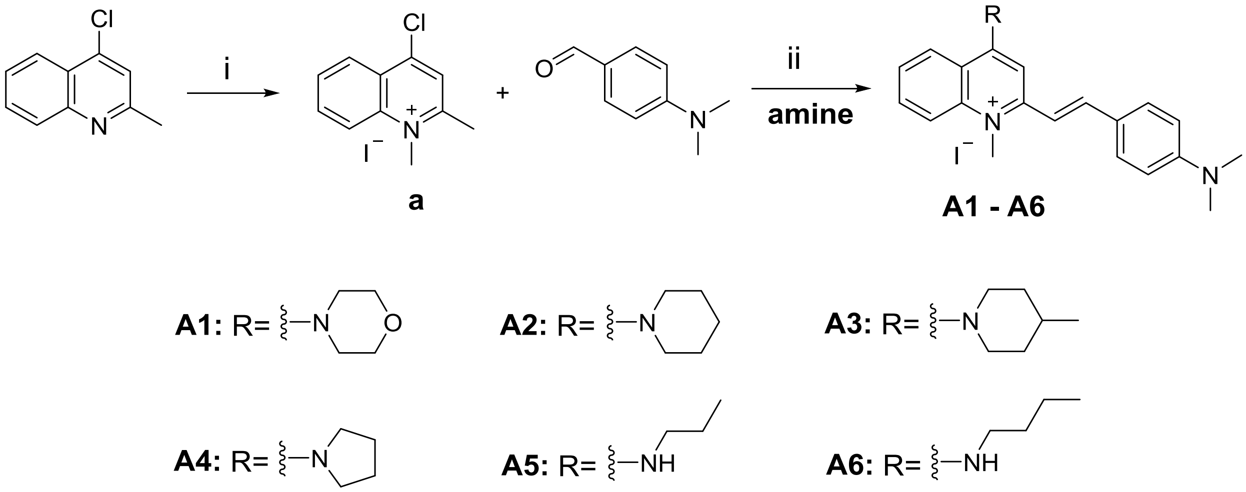

Scheme S1. Synthetic routes to **A1-A6** and their molecular structures. Reagents and conditions: (i) iodomethane, sulfolane, 60 °C, 2 h; (ii) The 3-compoent one-pot reaction of **a** with a selected amine (morpholine, piperidine, 4-methylpiperidine, pyrrolidine, propylamine, or butyl amine) and the aldehyde in *n*-butanol at 80 °C for 8 h.

1.2 The characterizations of A1–A6

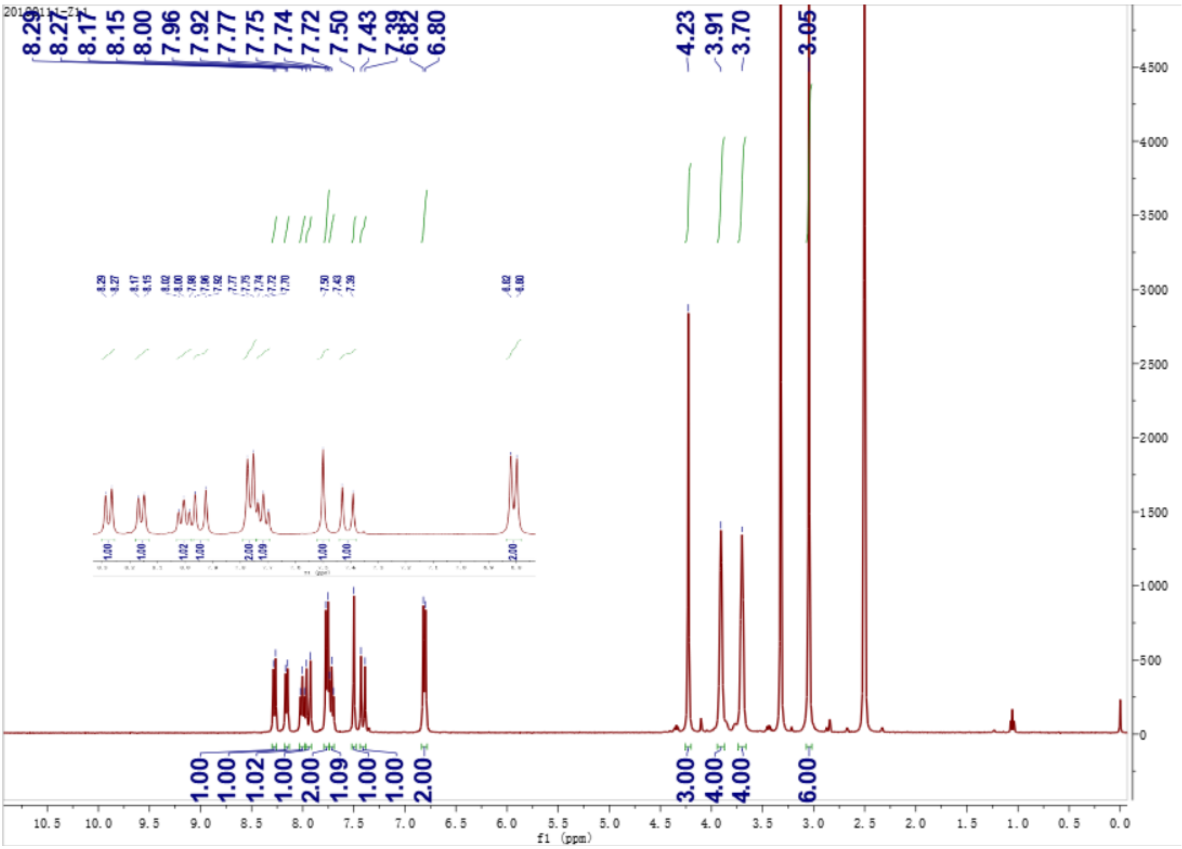

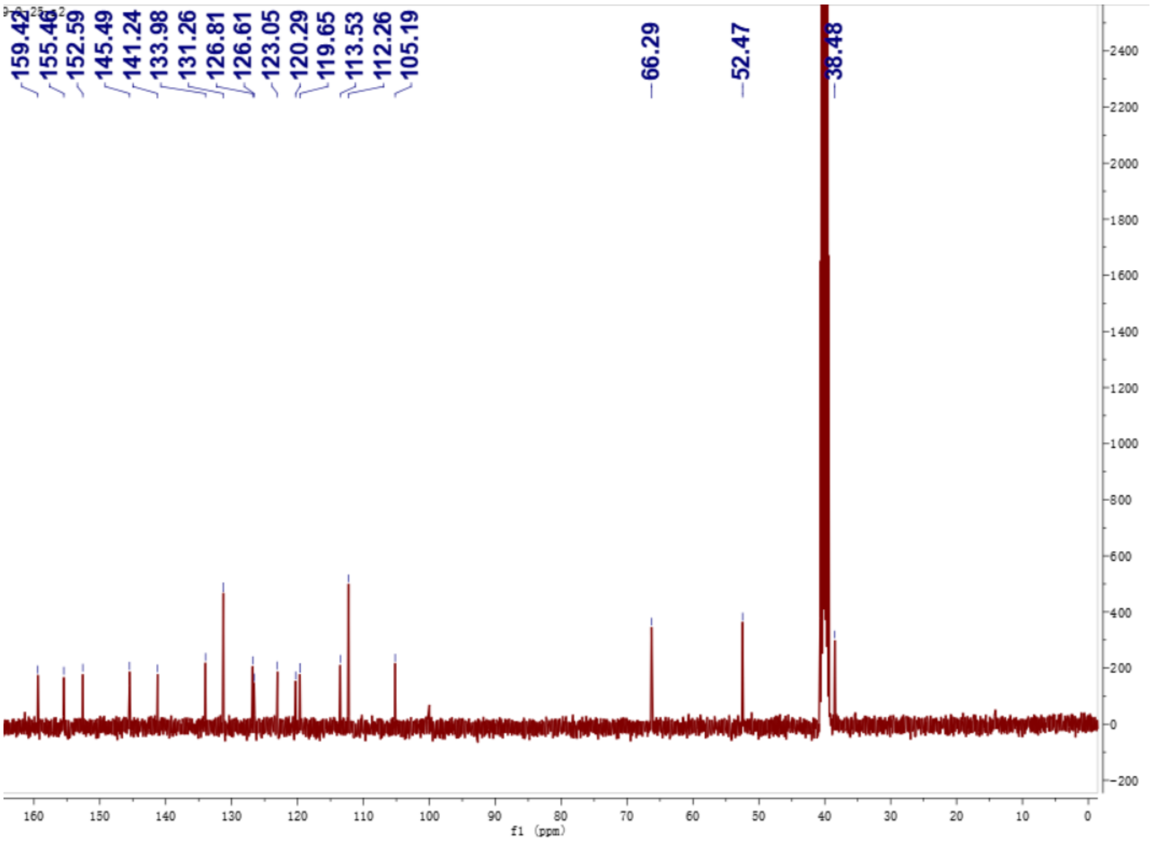

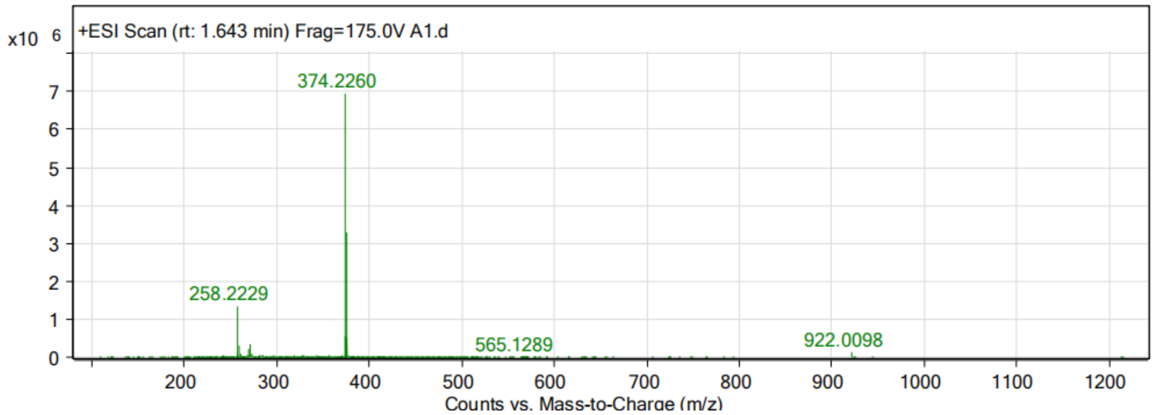

Fig. S1 ^{1}H NMR (DMSO-d_6), ^{13}C NMR (DMSO-d_6), HRMS of **A1**.

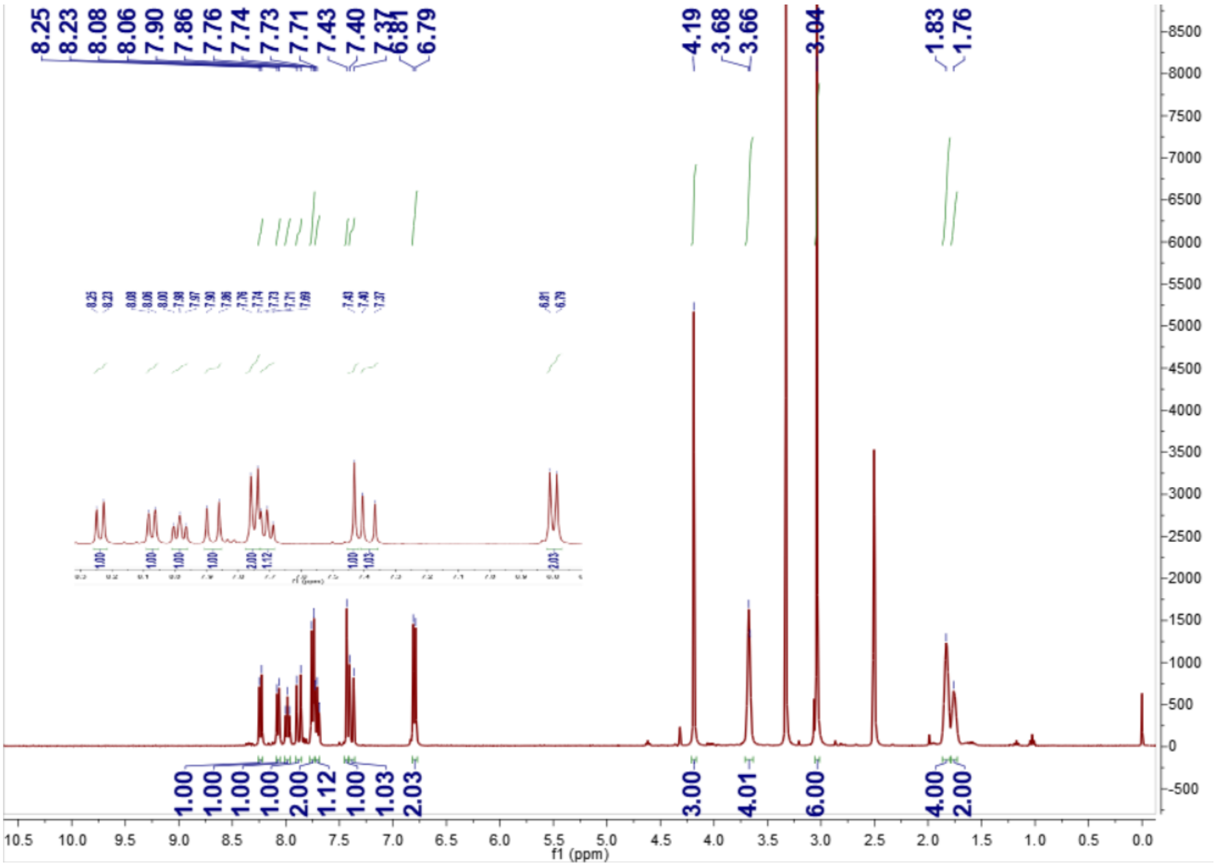

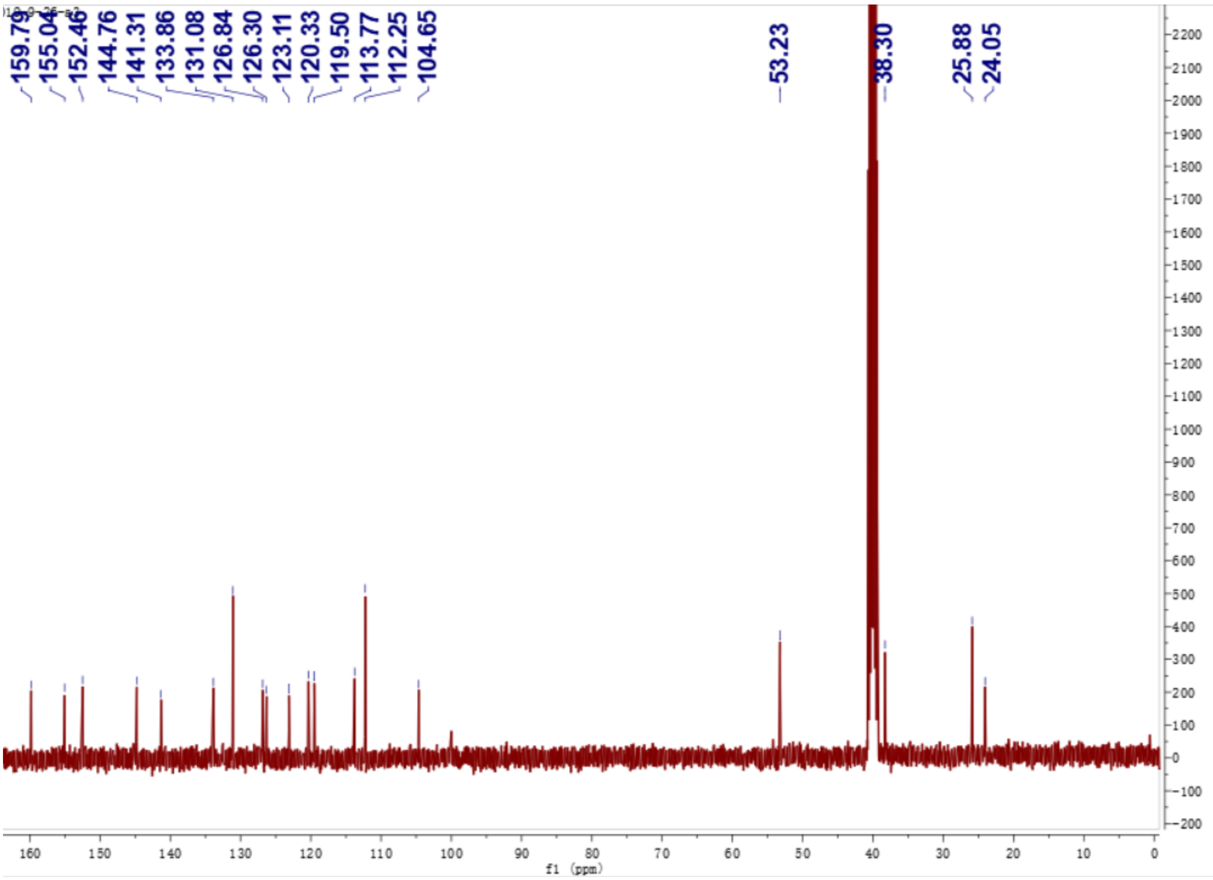

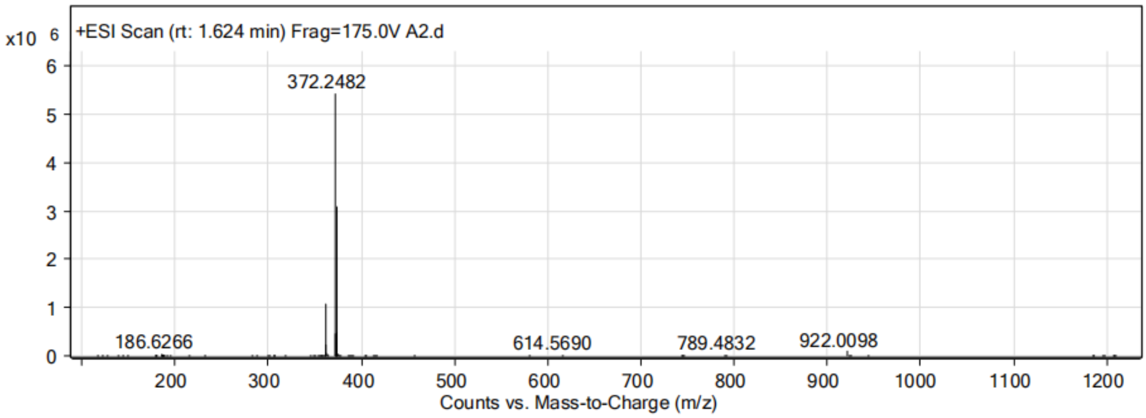

Fig. S2 ^{1}H NMR (DMSO-d_6), ^{13}C NMR (DMSO-d_6), HRMS of **A2**.

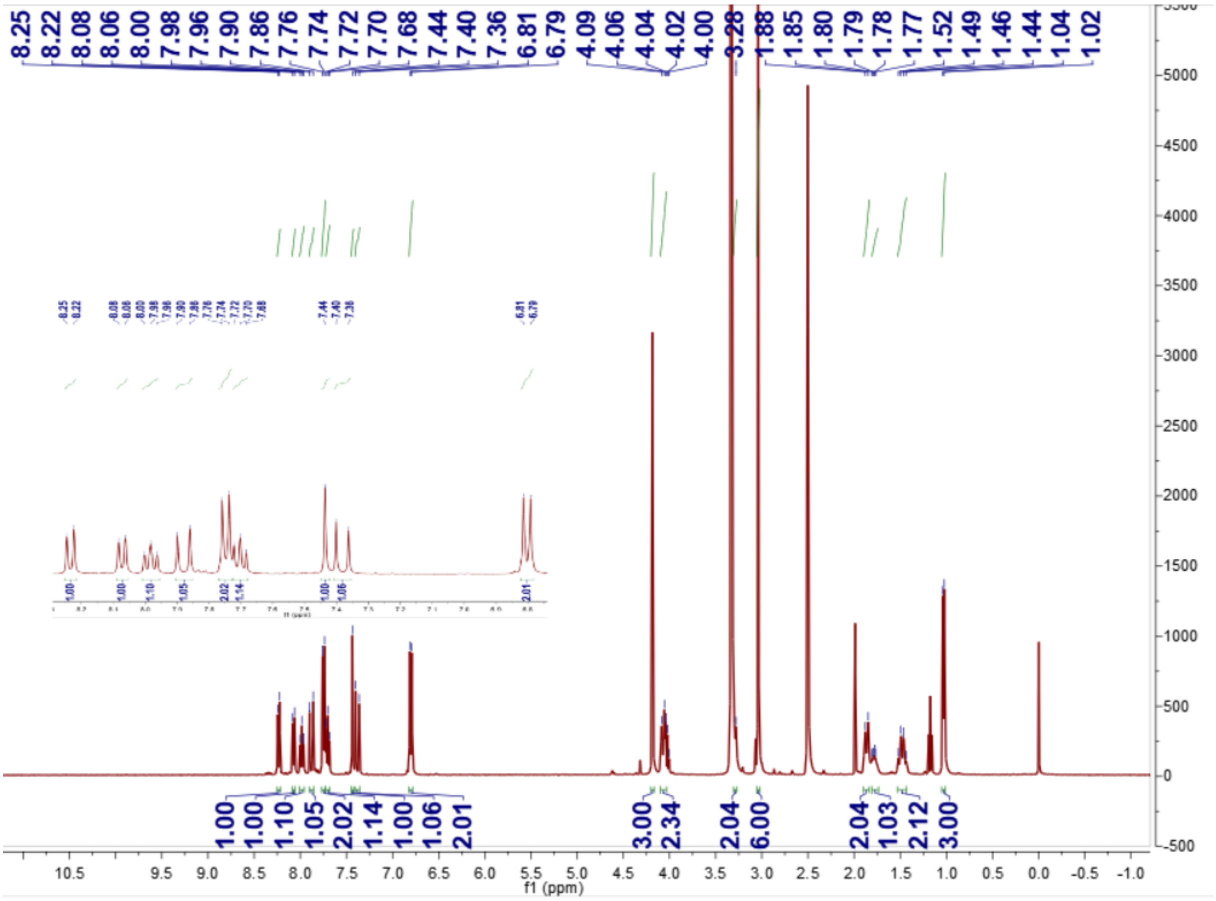
8.25
8.22
8.08
8.06
8.00
7.98
7.96
7.90
7.86
7.76
7.74
7.72
7.70
7.68
7.44
7.40
7.36
6.81
6.79
4.09
4.06
4.04
4.02
4.00
3.28
1.88
1.85
1.80
1.79
1.78
1.77
1.52
1.49
1.46
1.44
1.04
1.02
1.00
1.00
1.10
1.05
2.02
1.14
1.00
1.06
2.01
3.00
2.34
2.04
6.00
2.04
1.03
2.12
3.00
10.5
9.5
9.0
8.5
8.0
7.5
7.0
6.5
6.0
5.5
5.0
4.5
4.0
3.5
3.0
2.5
2.0
1.5
1.0
0.5
0.0
-0.5
-1.0
f1 (ppm)
5000
4500
4000
3500
3000
2500
2000
1500
1000
500
0
-500

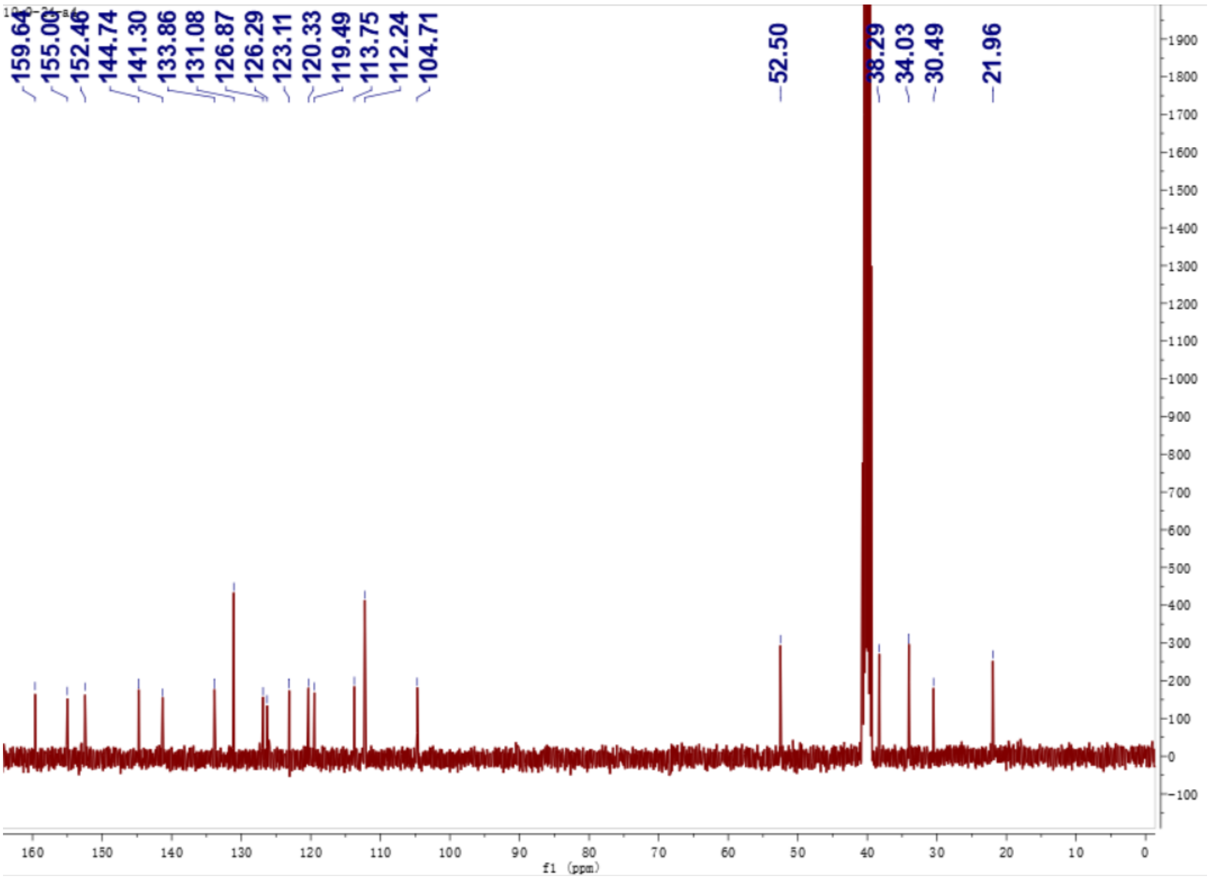
159.64
155.00
152.46
144.74
141.30
133.86
131.08
126.87
126.29
123.11
120.33
119.49
113.75
112.24
104.71
52.50
38.29
34.03
30.49
21.96
160
150
140
130
120
110
100
90
80
70
60
50
40
30
20
10
0
f1 (ppm)
1900
1800
1700
1600
1500
1400
1300
1200
1100
1000
900
800
700
600
500
400
300
200
100
0
-100

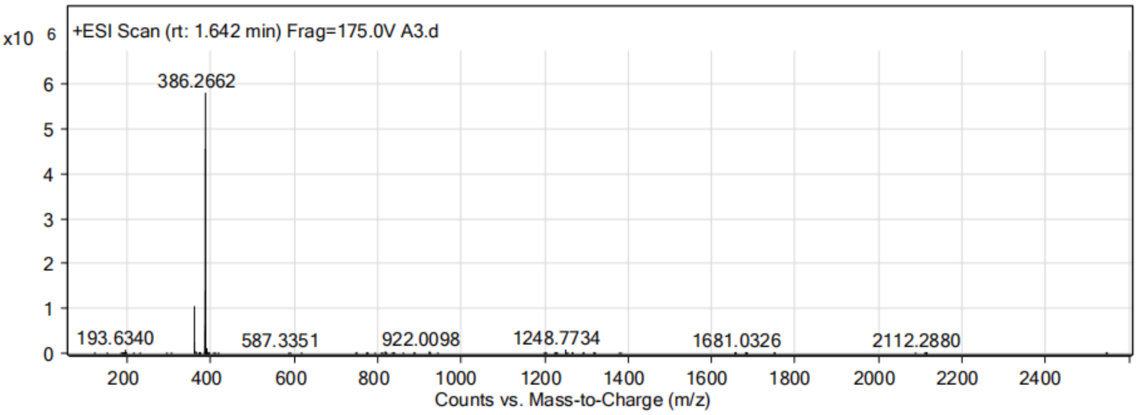

Fig. S3 ^{1}H NMR (DMSO-d_6), ^{13}C NMR (DMSO-d_6), HRMS of **A3**.

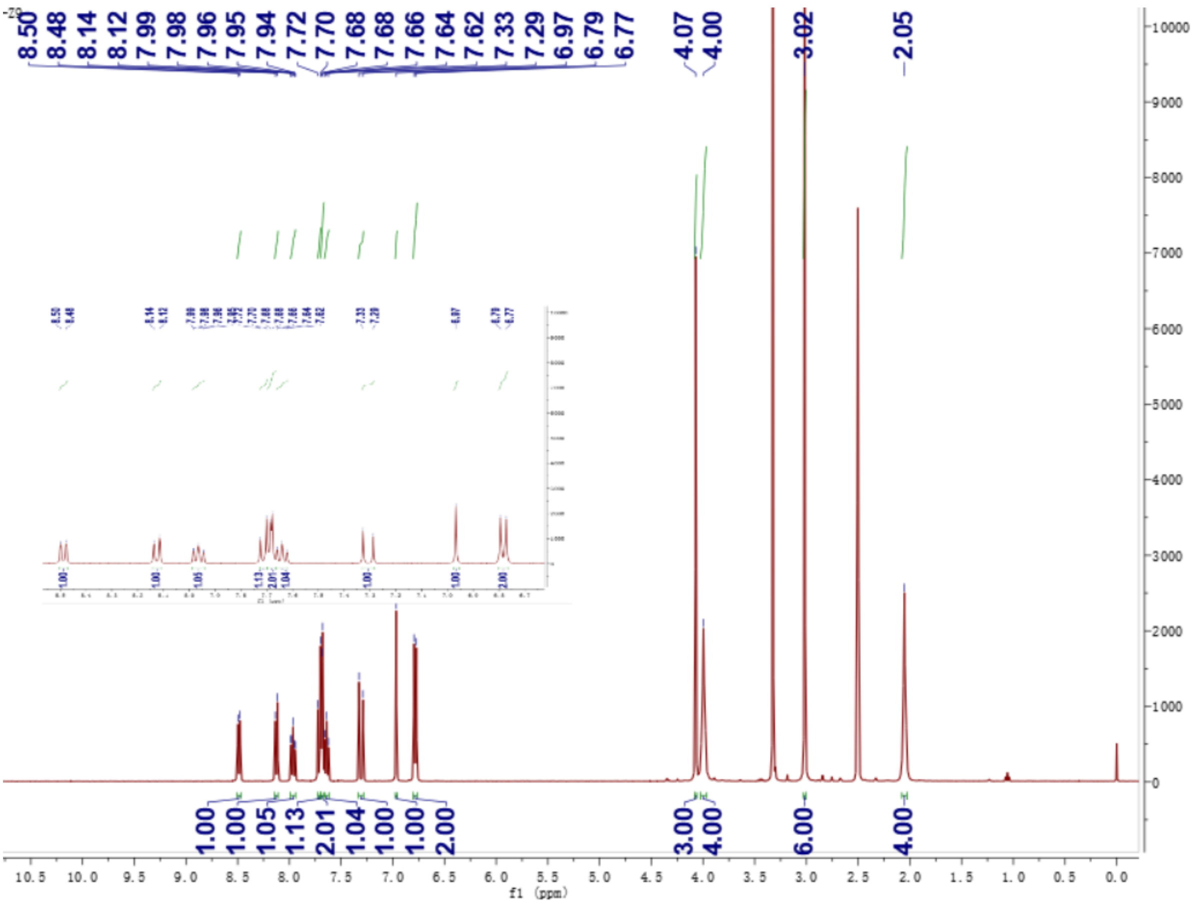

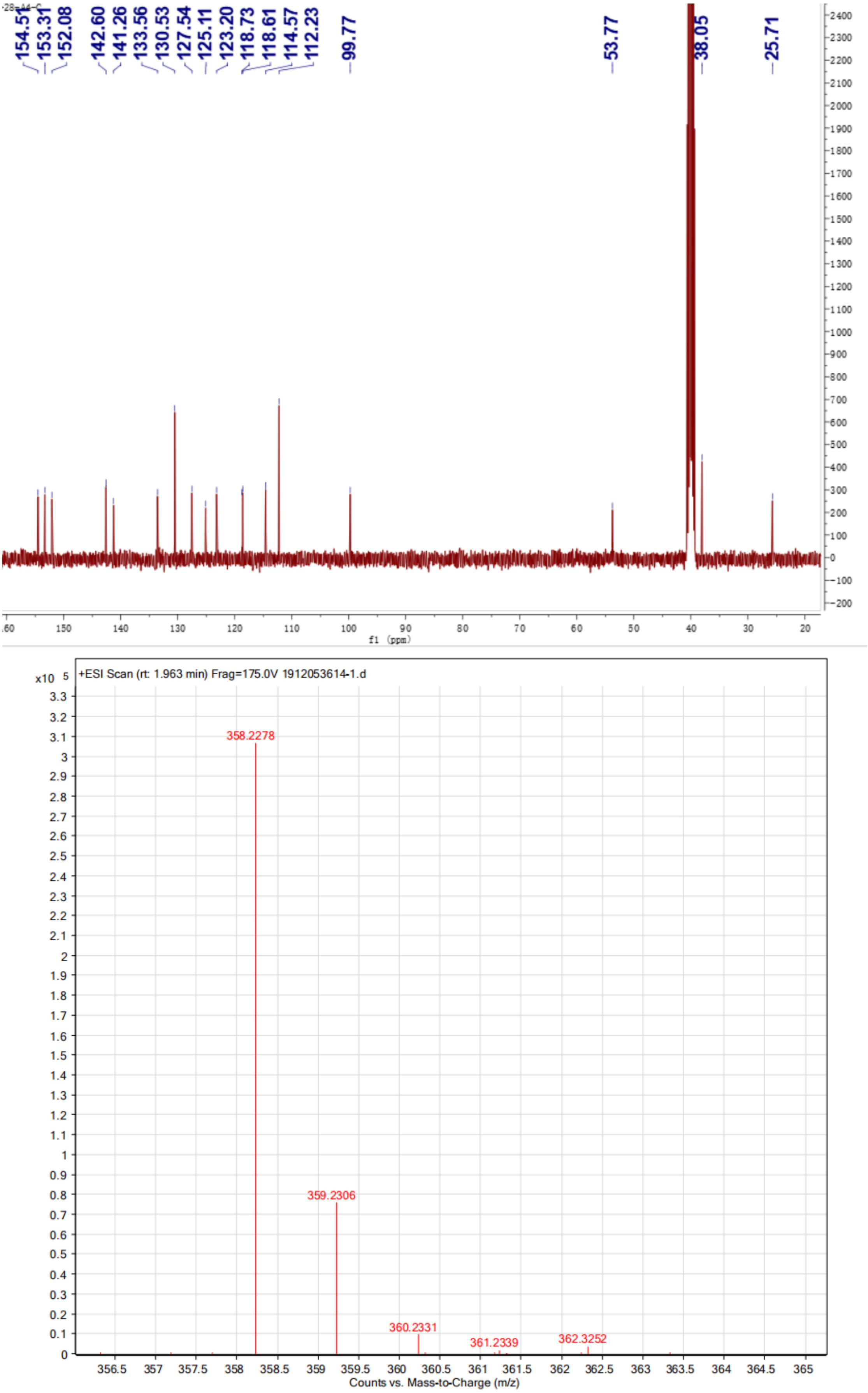

Fig. S4 ^{1}H NMR (DMSO-d_6), ^{13}C NMR (DMSO-d_6), HRMS of **A4**.

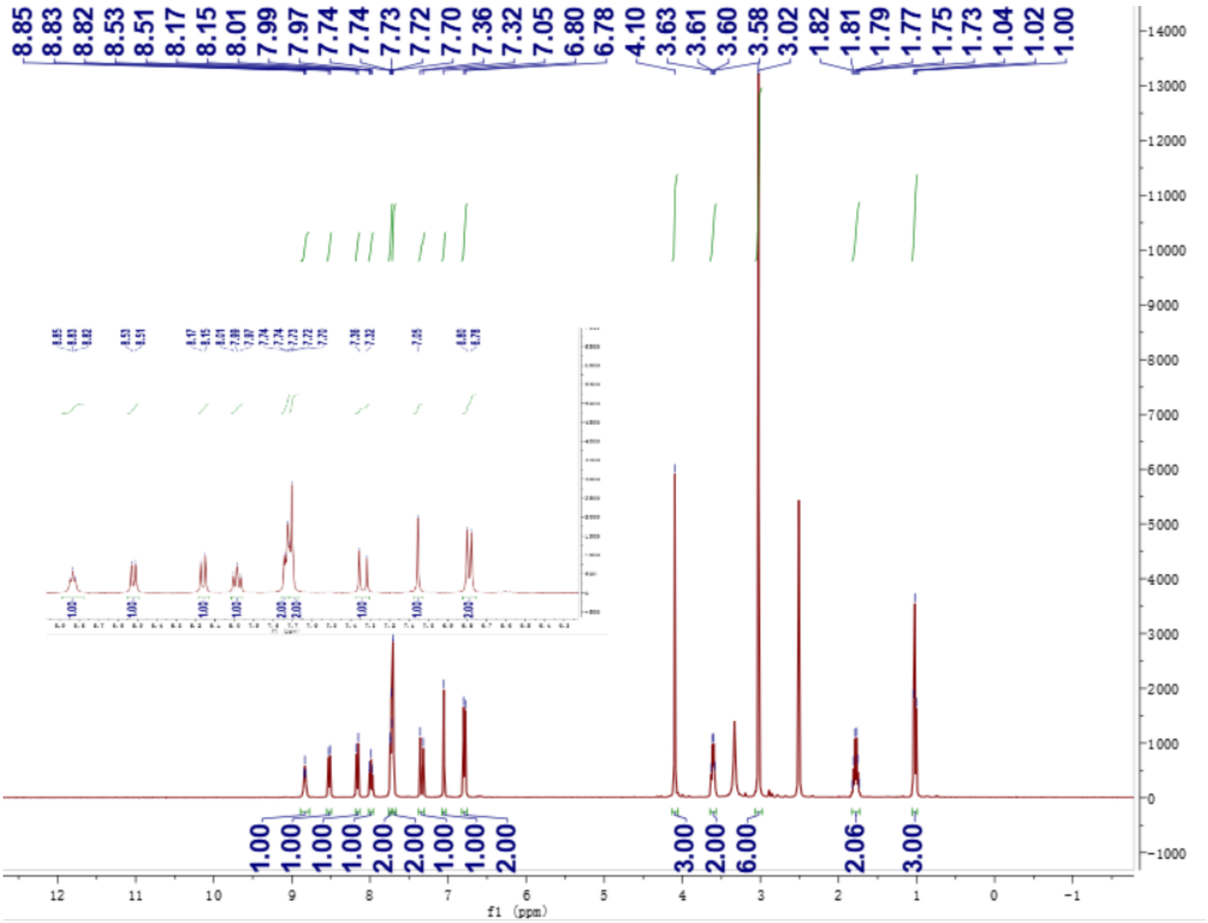
8.85
8.83
8.82
8.53
8.51
8.17
8.15
8.01
7.99
7.97
7.74
7.74
7.73
7.72
7.70
7.36
7.32
7.05
6.80
6.78
4.10
3.63
3.61
3.60
3.58
3.02
1.82
1.81
1.79
1.77
1.75
1.73
1.04
1.02
1.00
1.00
1.00
1.00
1.00
2.00
2.00
1.00
1.00
2.00
3.00
2.00
6.00
2.06
3.00
f1 (ppm)

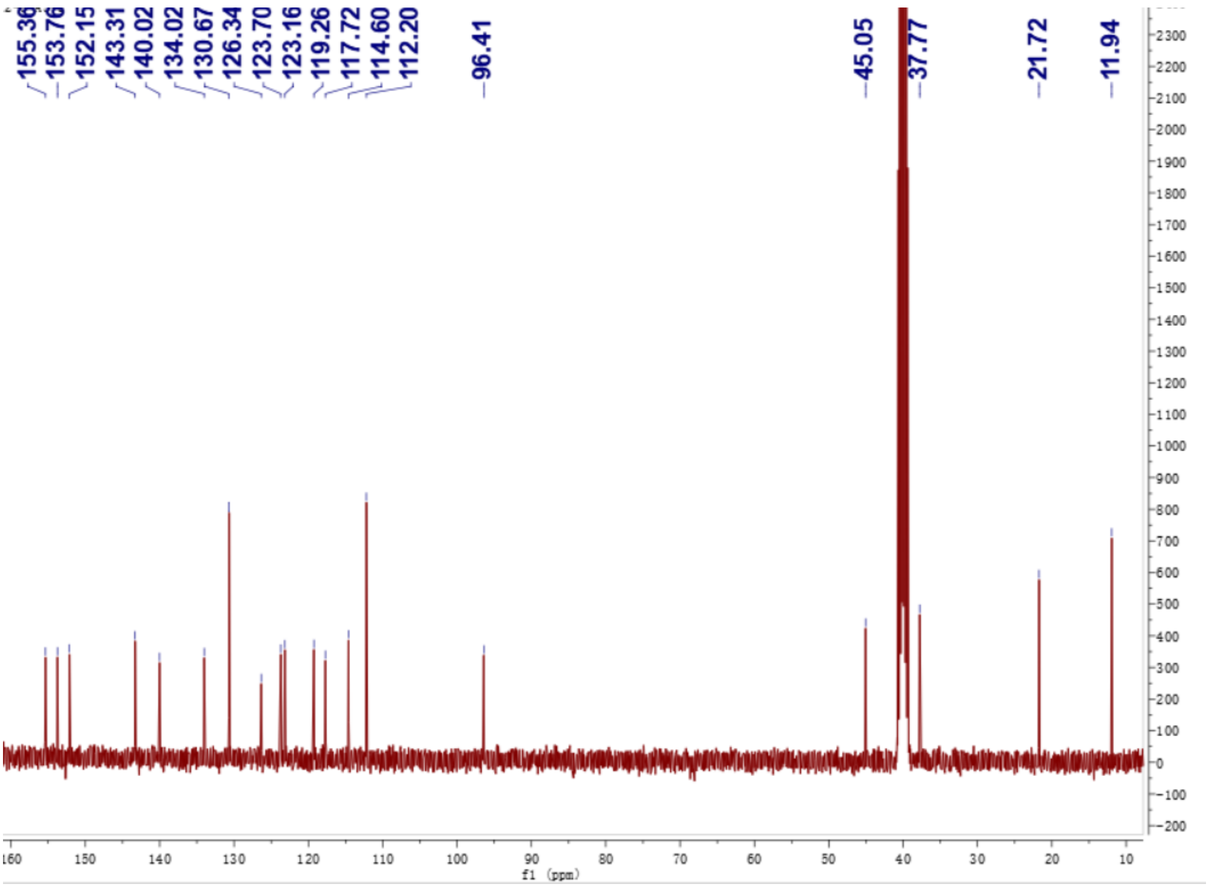
155.36
153.76
152.15
143.31
140.02
134.02
130.67
126.34
123.70
123.16
119.26
117.72
114.60
112.20
96.41
45.05
37.77
21.72
11.94
f1 (ppm)

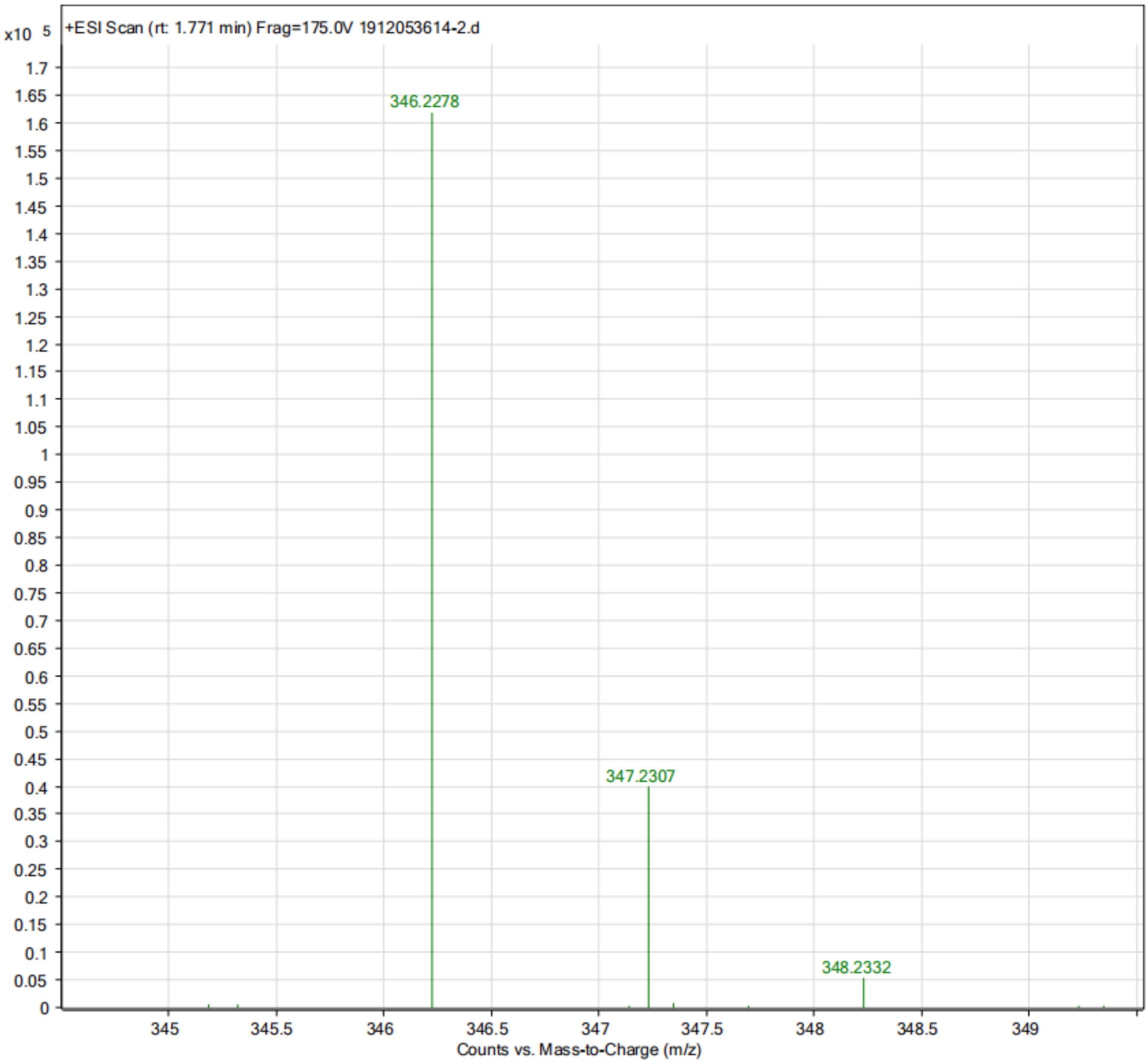

Fig. S5 ^{1}H NMR (DMSO-d_6), ^{13}C NMR (DMSO-d_6), HRMS of **A5**.

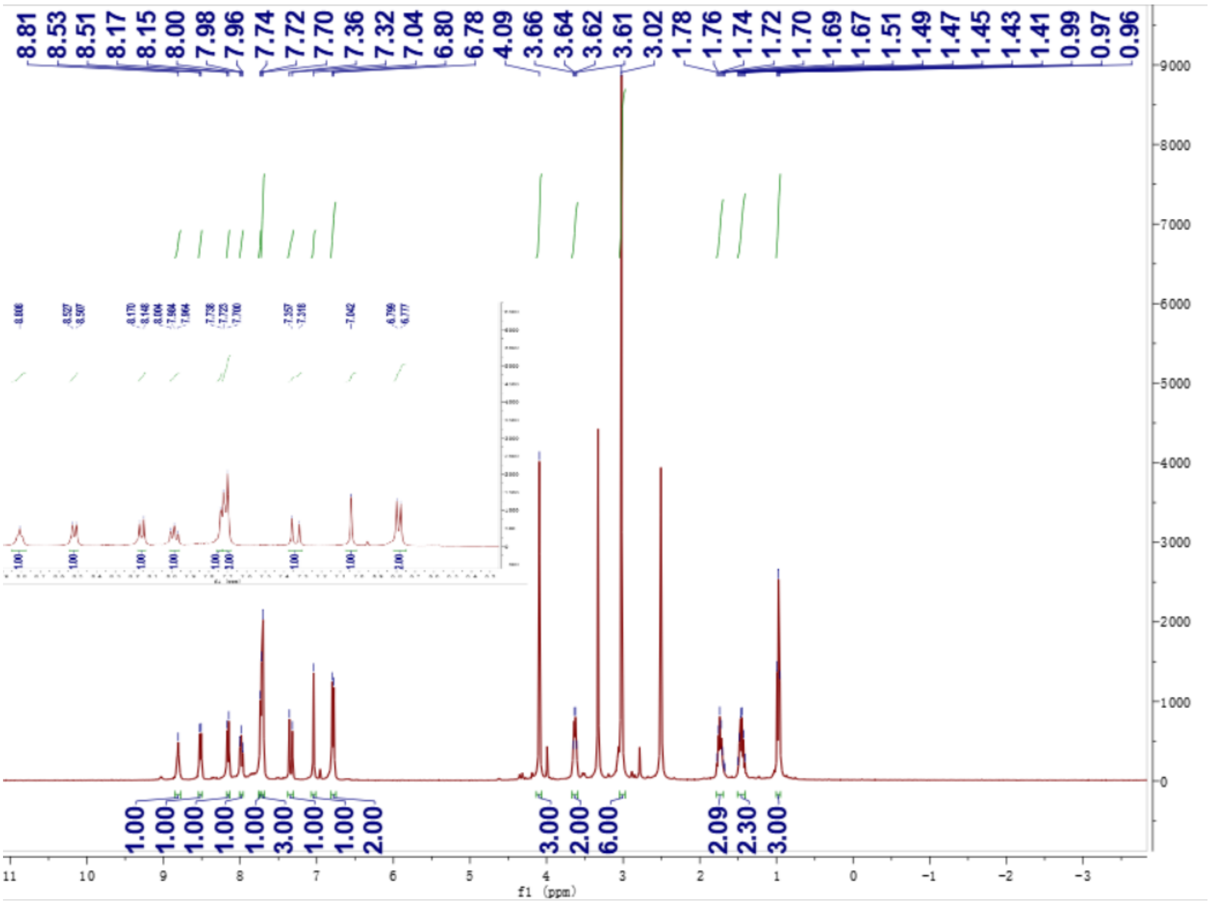
8.81
8.53
8.51
8.17
8.15
8.00
7.98
7.96
7.74
7.72
7.70
7.36
7.32
7.04
6.80
6.78
4.09
3.66
3.64
3.62
3.61
3.02
1.78
1.76
1.74
1.72
1.70
1.69
1.67
1.51
1.49
1.47
1.45
1.43
1.41
0.99
0.97
0.96
1.00
1.00
1.00
1.00
1.00
3.00
1.00
1.00
2.00
3.00
2.00
6.00
2.09
2.30
3.00
f1 (ppm)

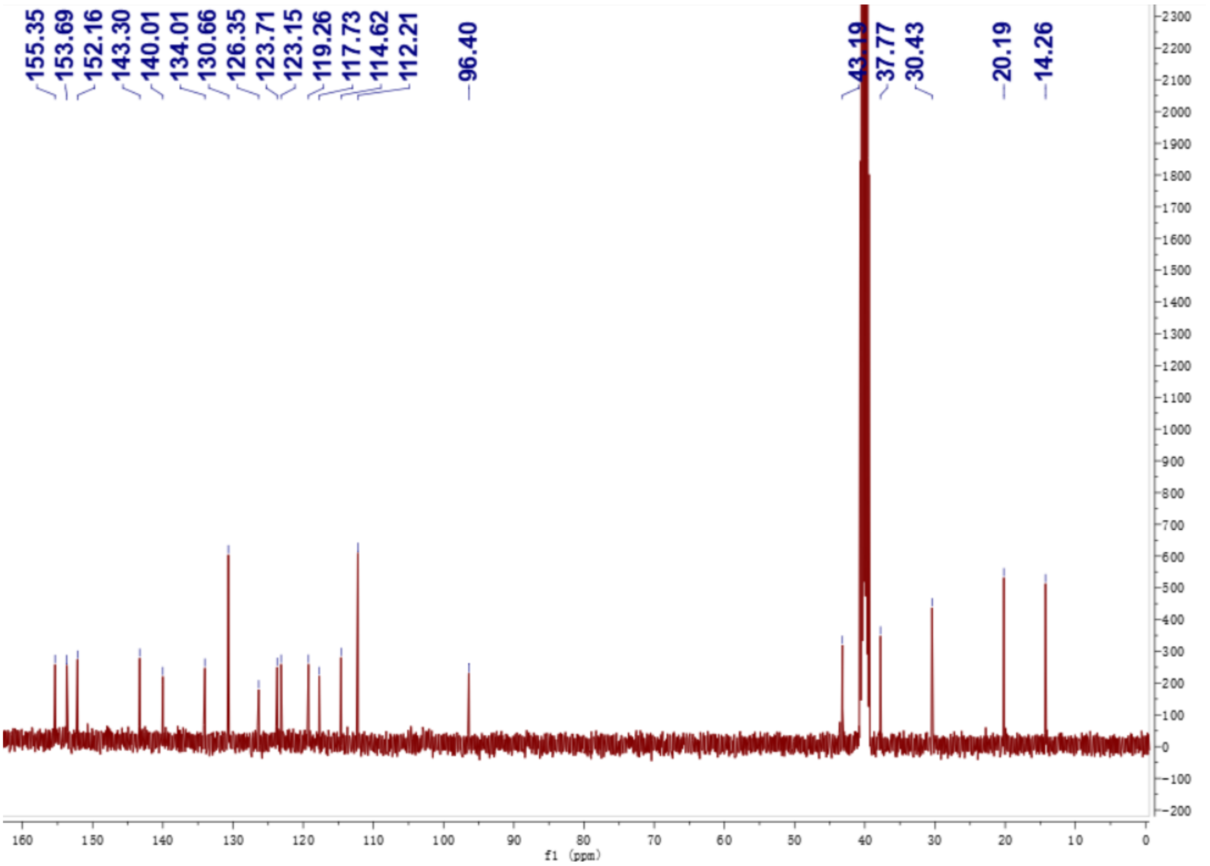
155.35
153.69
152.16
143.30
140.01
134.01
130.66
126.35
123.71
123.15
119.26
117.73
114.62
112.21
96.40
43.19
37.77
30.43
20.19
14.26
f1 (ppm)

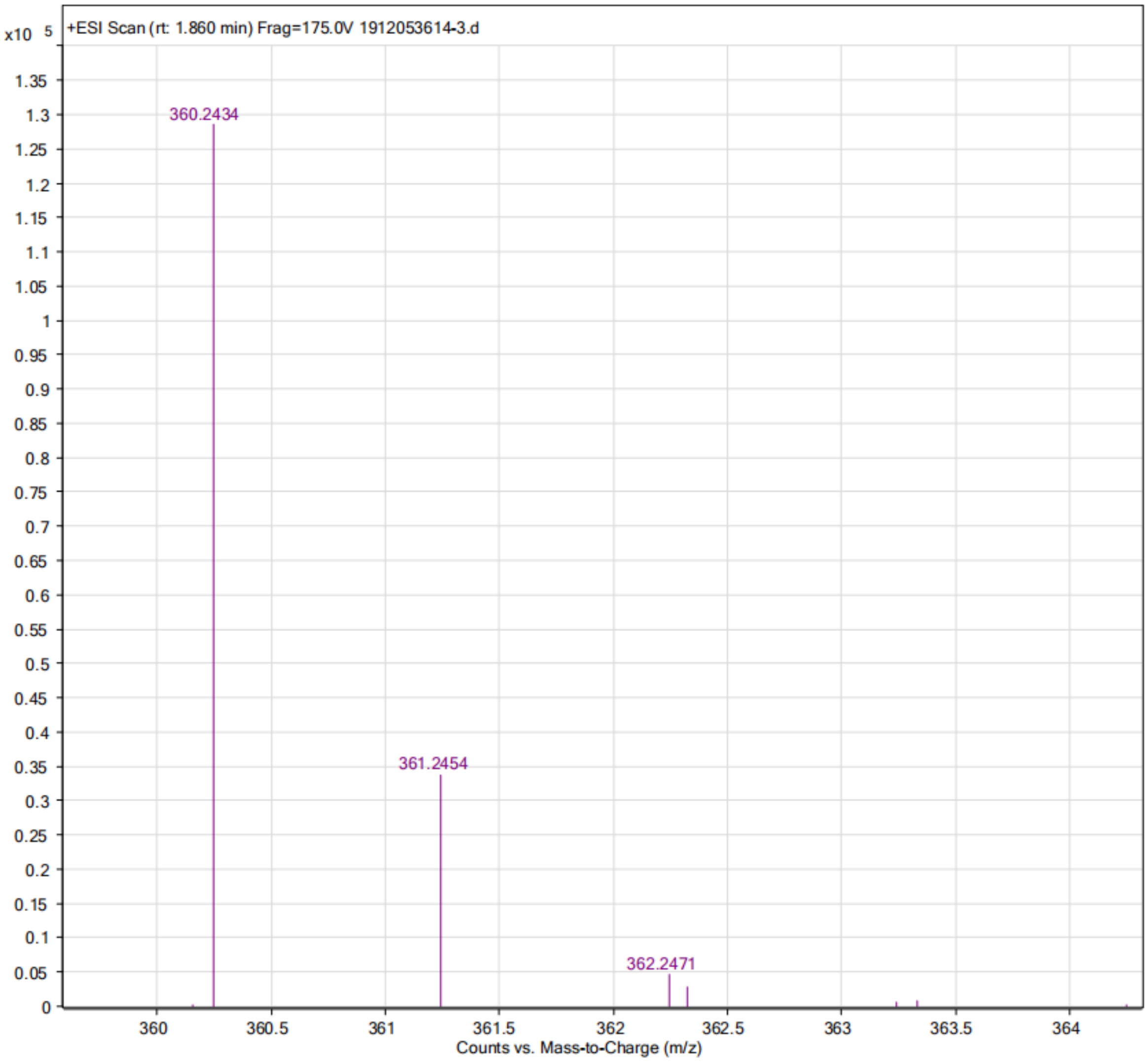

Fig. S6 ^{1}H NMR (DMSO-d_6), ^{13}C NMR (DMSO-d_6), HRMS of **A6**.

2. List of Supporting Table, Spectra and Graphs

Table S1. Sequences of oligonucleotides used in the present study.

Abbreviation	Sequence/Source	Structure/origin
RNA	Ribonucleic acid from Baker's yeast	Single-stranded
da21	AAAAAAAAAAAAAAAAAAAAA	Single-stranded
dt21	TTTTTTTTTTTTTTTTTTTTT	Single-stranded
4at	ATATATATATAT	Duplex
ds12	GCGCAATTGCGC	Duplex
ds26	CAATCGGATCGAATTCGATCCGATTG	Duplex
hairpin	CGCGCGCGTTTTCGCGCGCG	Duplex
ckit1	AGGGAGGGCGCTGGGAGGAGGG	Promoter G-quadruplex
ckit2	GGGCGGGCGCGAGGGAGGGG	Promoter G-quadruplex
pu18	AGGGTGGGGAGGGTGGGG	Promoter G-quadruplex
pu22	TGAGGGTGGGTAGGGTGGGTAA	Promoter G-quadruplex
pu27	TGGGGAGGGTGGGGAGGGTGGGGAAGG	Promoter G-quadruplex
bcl2	GGGCGCGGGAGGAAGGGGGCGGG	Promoter G-quadruplex
Hras	TCGGGTTGCGGGCGCAGGGCACGGGCG	Promoter G-quadruplex
Kras	GGGCGGTGTGGGAAGAGGGAAGAGGGG	Promoter G-quadruplex
VEGF	GGGGCGGGCCGGGGGCGGGG	Promoter G-quadruplex
RET	GGGGCGGGGCGGGGCGGGGG	Promoter G-quadruplex
telo21	GGGTTAGGGTTAGGGTTAGGG	Telomere G-quadruplex
htg22	AGGGTTAGGGTTAGGGTTAGGG	Telomere G-quadruplex
oxy12	GGGGTTTTGGGG	Telomere G-quadruplex
human12	TTAGGGTTAGGG	Telomere G-quadruplex
Htg24	TTGGGTTAGGGTTAGGGTTAGGGA	Telomere G-quadruplex

Table S2. Equilibrium binding constant (*K*) of the probe with the Double-stranded DNA ds26 at 25 °C.[a]

Probe[a]	*K* ($\times 10^6$ M^{-1})
A1	—
A2	0.61
A3	0.57
A4	0.56
A5	1.74
A6	2.15

[a] Concentration of the probe used was 5.0 μM, the final concentration of pu27 was 9.0 μM.

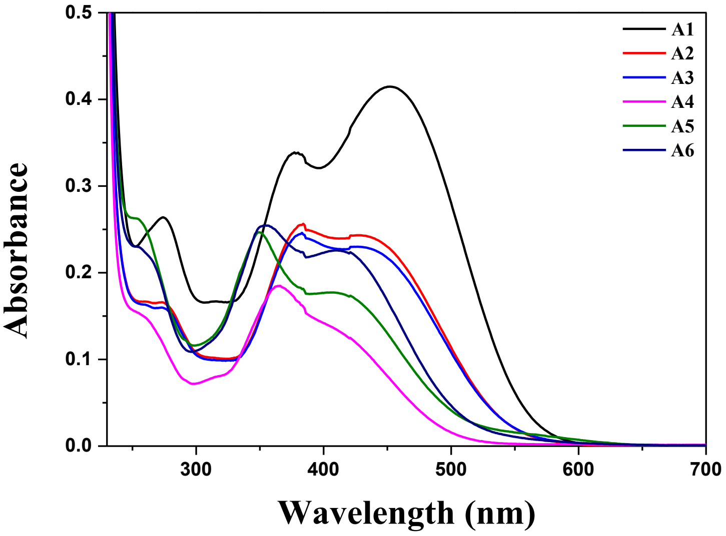

Fig. S7 UV-vis spectra of probes **A1-A6** in Tris buffer (10 mM Tris-HCl buffer containing 60 mM KCl). The concentration of the probes used was 15 μM.

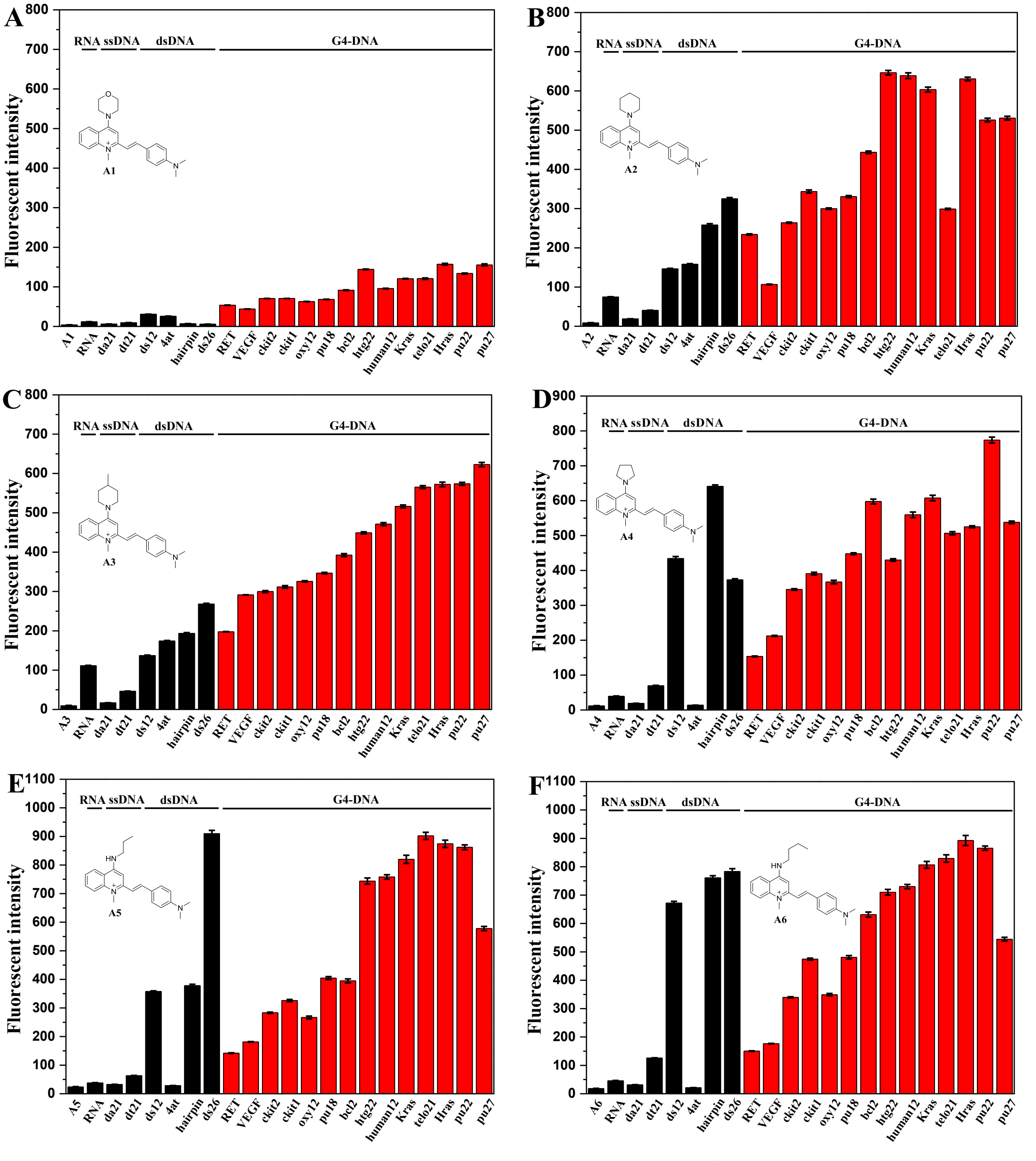

Fig. S8 The fluorescence intensity of the probes **A1-A6** in sensing with different DNA and RNA. Single-stranded DNA: da21, dt21; duplex DNA: 4at, ds12, ds26, hairpin; G-quadruplex DNA: ckit1, ckit2, pu18, pu22, pu27, bcl2, telo21, htg22, oxy12, human12, Hras, Kras, VEGF and RET. The concentration of the probes was 5 μM in a Tris-HCl buffer containing 60 mM KCl. The concentrations of DNA and RNA are used at the maximum of the fluorescent signal enhancement (9.0 μM).

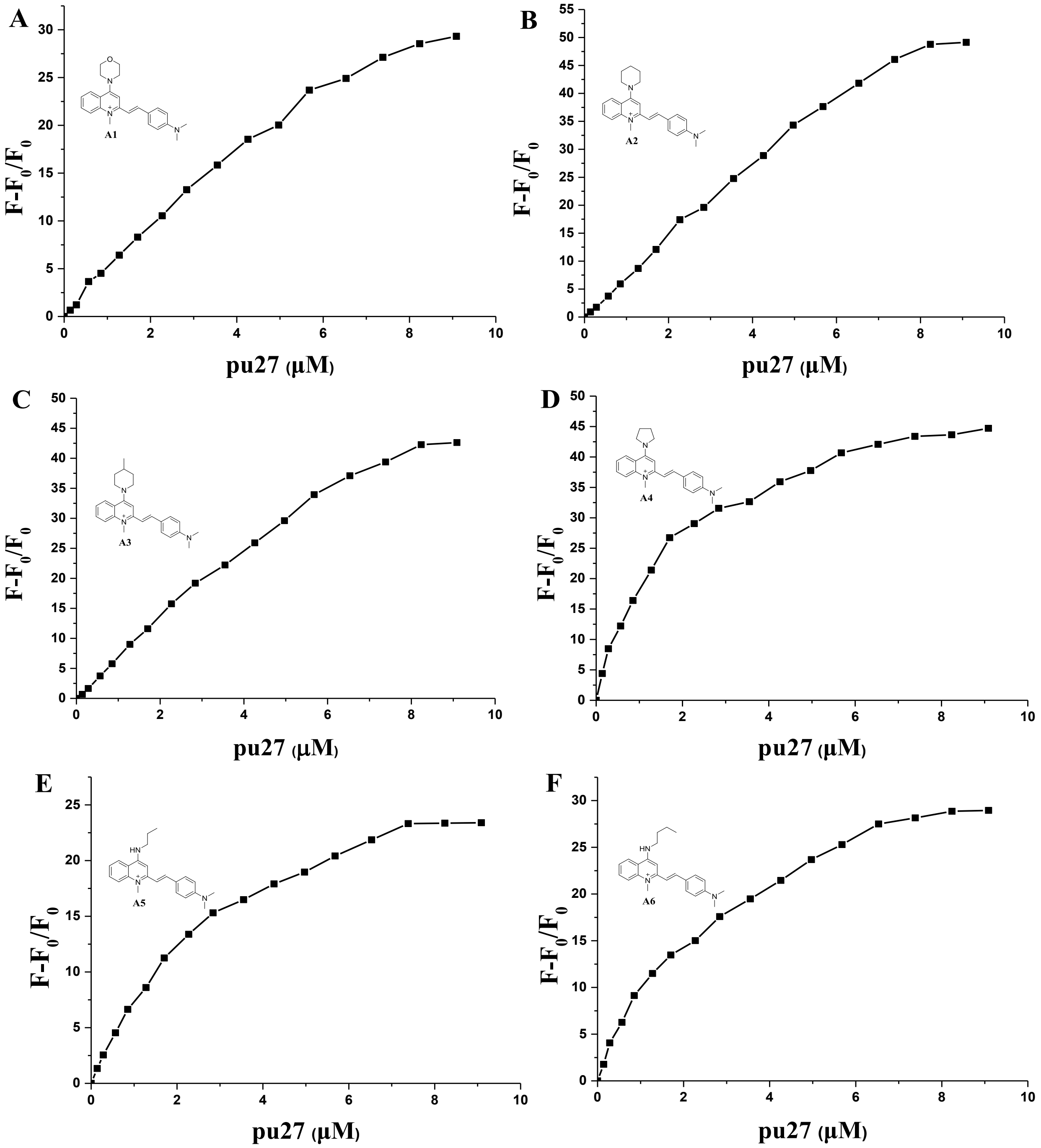

Fig. S9 The fluorescence titration of probes **A1-A6** (5 μM) with stepwise addition of G-quadruplex pu27 (0–9.0 μM). F_0 represents the fluorescence intensity without pu27 and F represents the fluorescence intensity after adding pu27.

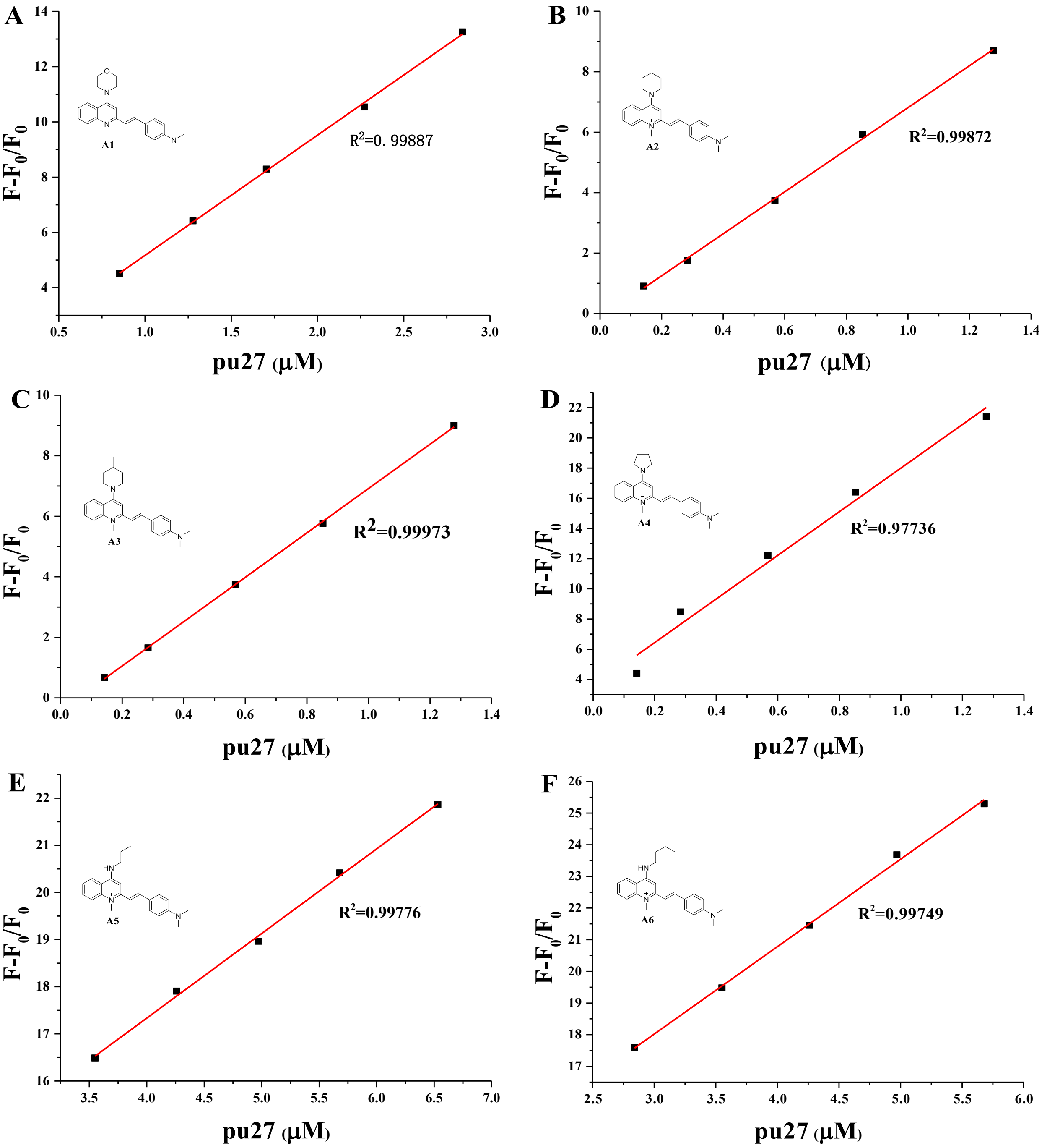

Fig. S10 Linear detection range of probes **A1-A6** in the biosensing of pu27.

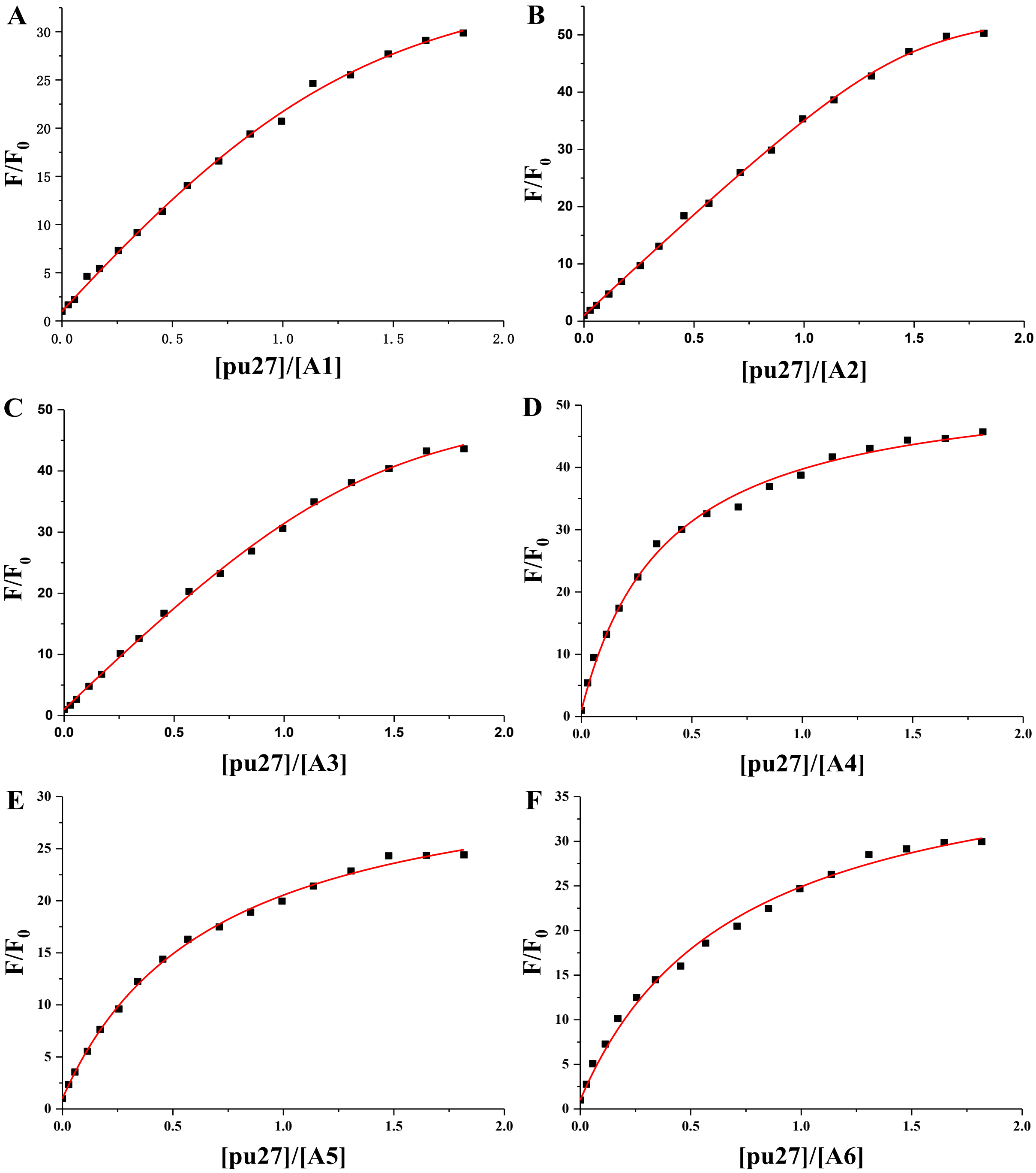

Fig. S11 Fluorescence titrations, presented as a relative increase of the integral fluorescence (F/F$_0$) of pu27 with **A1-A6** (5 μM) in 10 mM Tris-HCl buffer (pH 7.4, containing 60 mM KCl).

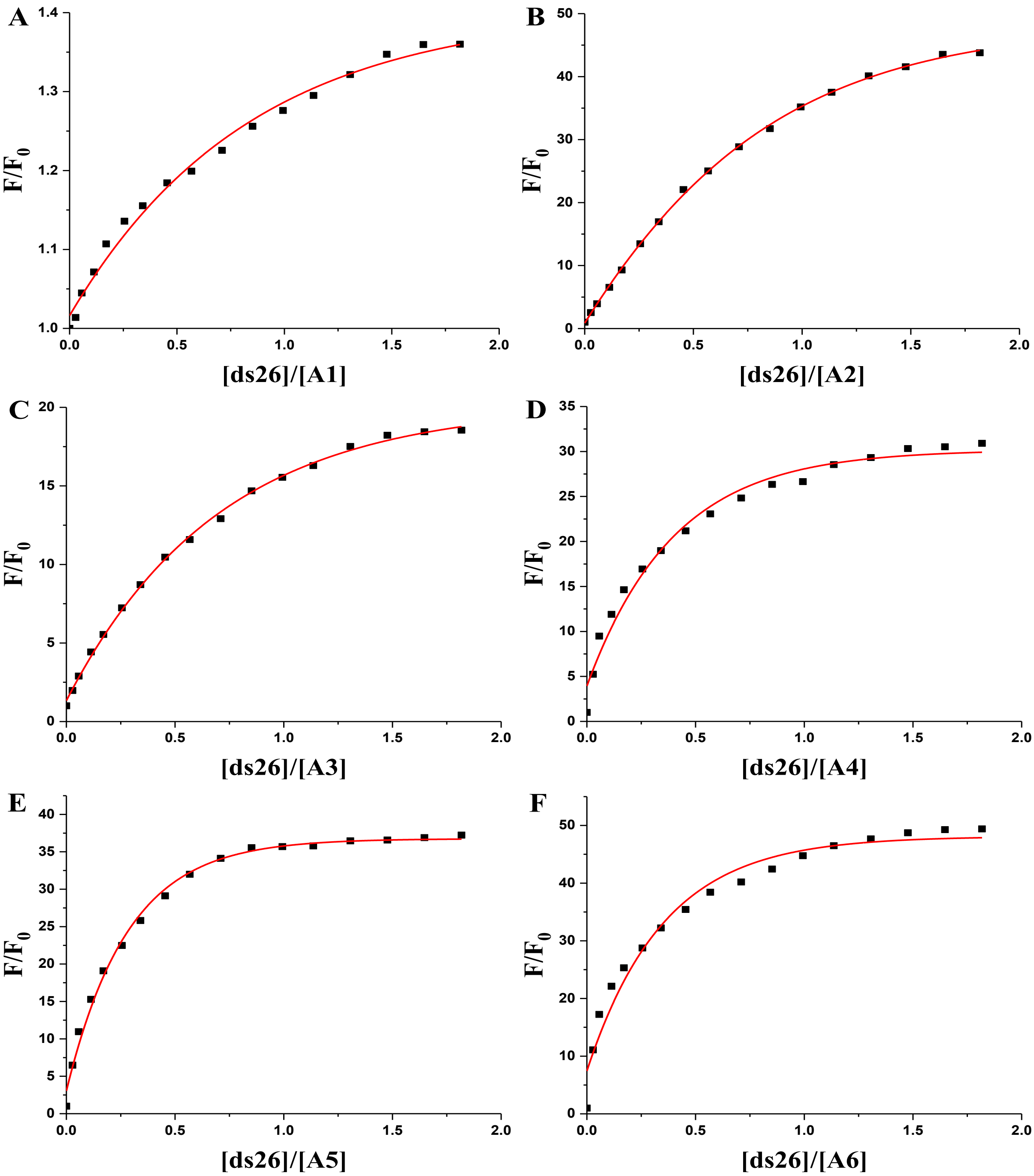

Fig. S12 Fluorescence titrations, presented as a relative increase of the integral fluorescence (F/F_0) of ds26 with **A1-A6** (5 μM) in 10 mM Tris-HCl buffer (pH 7.4, containing 60 mM KCl).

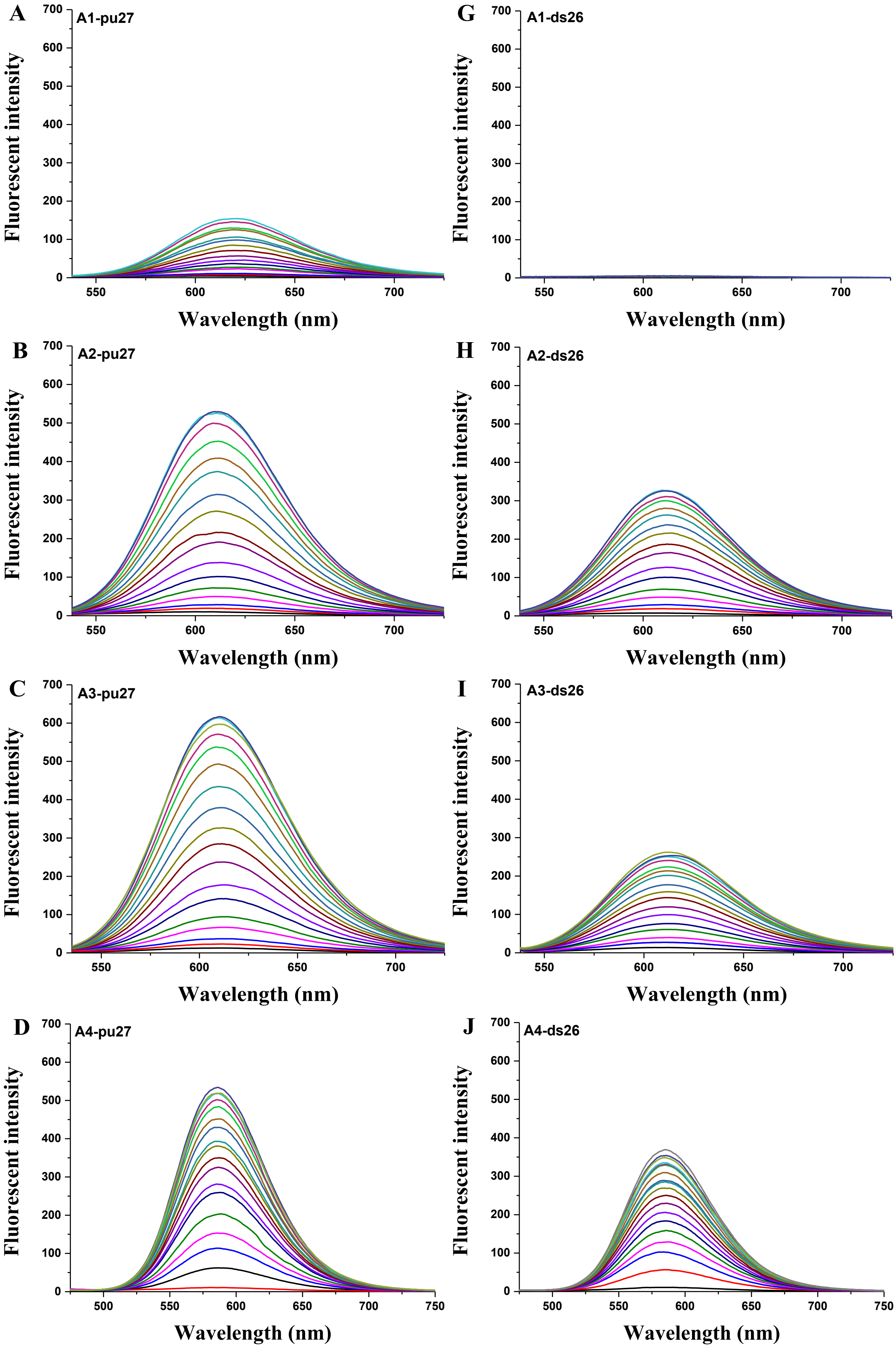
A
A1-pu27
G
A1-ds26
B
A2-pu27
H
A2-ds26
C
A3-pu27
I
A3-ds26
D
A4-pu27
J
A4-ds26
Fluorescent intensity
Wavelength (nm)
0
100
200
300
400
500
600
700
500
550
600
650
700
750

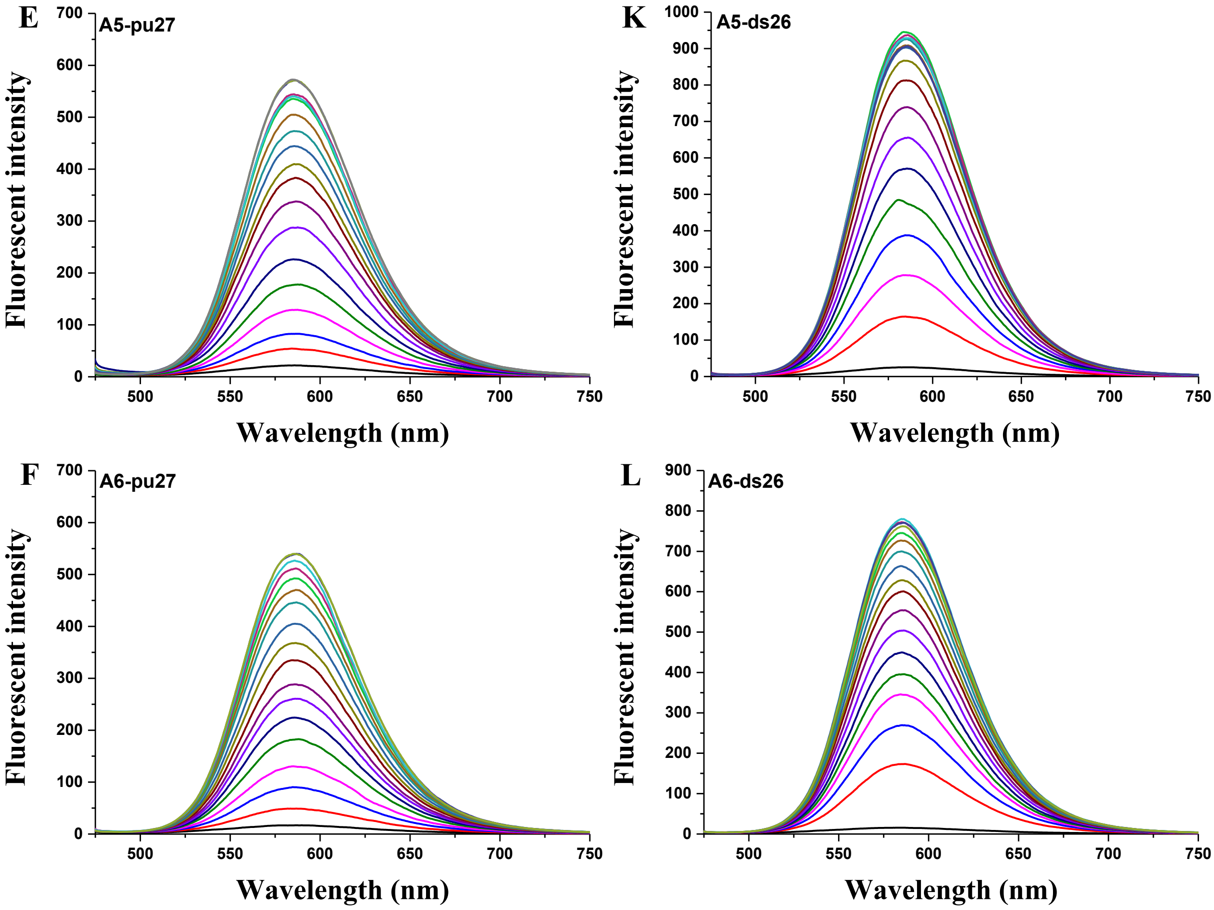

Fig. S13 Fluorescence titration spectra of probes **A1-A6** with pu27 or ds26 in a Tris-HCl buffer (10 mM, pH 7.4) containing 60 mM KCl. Fluorescence signal was measured at 25 °C. The concentration of the probes **A1-A6** used was 5 μM.

A

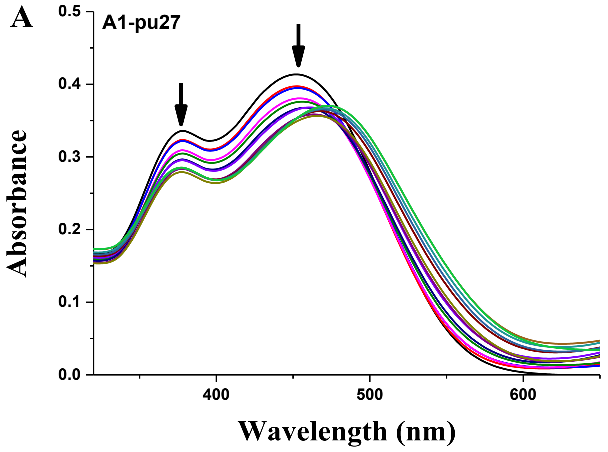
A1-pu27
Absorbance
0.0
0.1
0.2
0.3
0.4
0.5
400
500
600
Wavelength (nm)

G

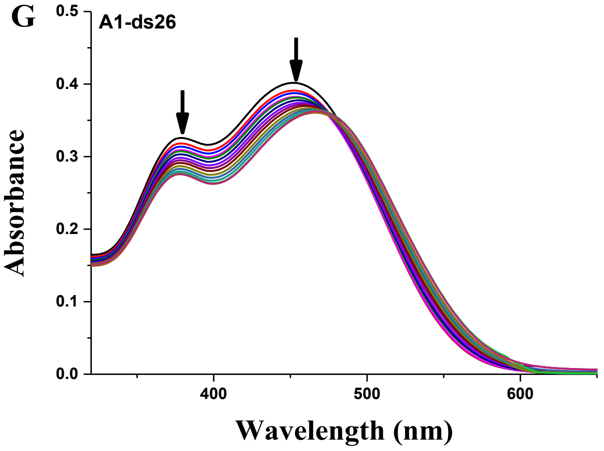
A1-ds26
Absorbance
0.0
0.1
0.2
0.3
0.4
0.5
400
500
600
Wavelength (nm)

B

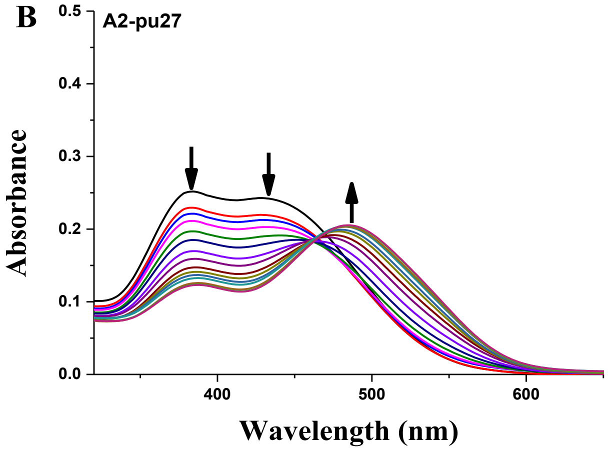
A2-pu27
Absorbance
0.0
0.1
0.2
0.3
0.4
0.5
400
500
600
Wavelength (nm)

E

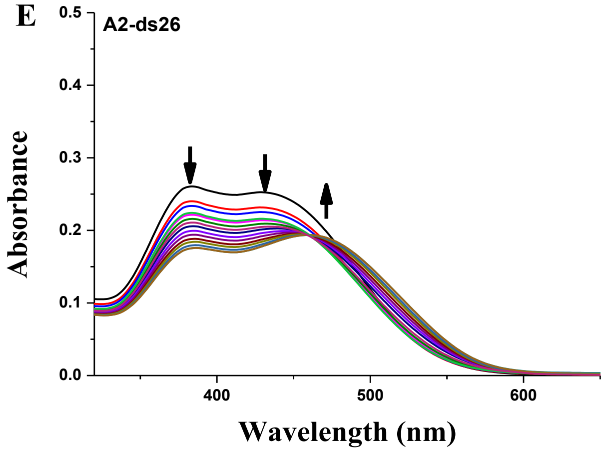
A2-ds26
Absorbance
0.0
0.1
0.2
0.3
0.4
0.5
400
500
600
Wavelength (nm)

C

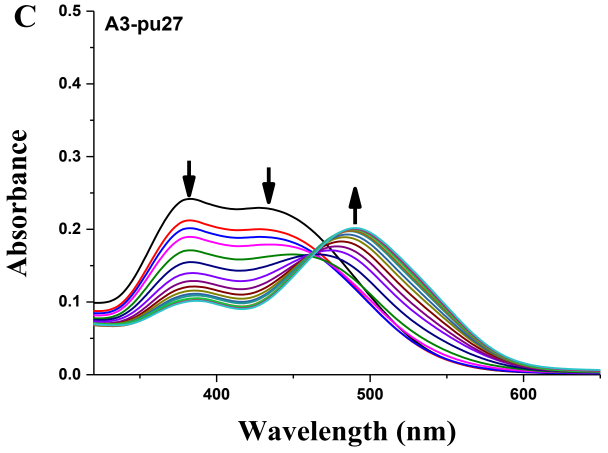
A3-pu27
Absorbance
0.0
0.1
0.2
0.3
0.4
0.5
400
500
600
Wavelength (nm)

I

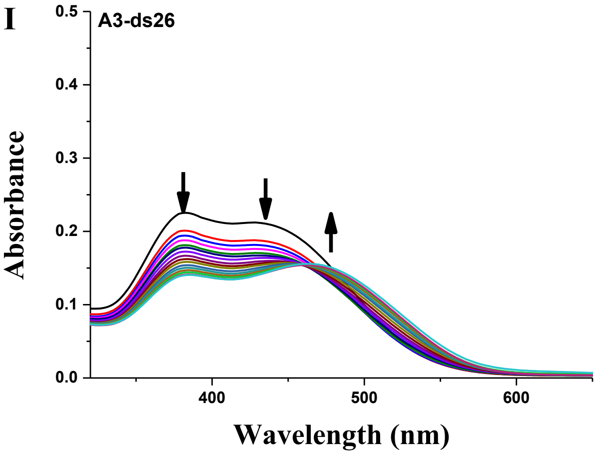
A3-ds26
Absorbance
0.0
0.1
0.2
0.3
0.4
0.5
400
500
600
Wavelength (nm)

D

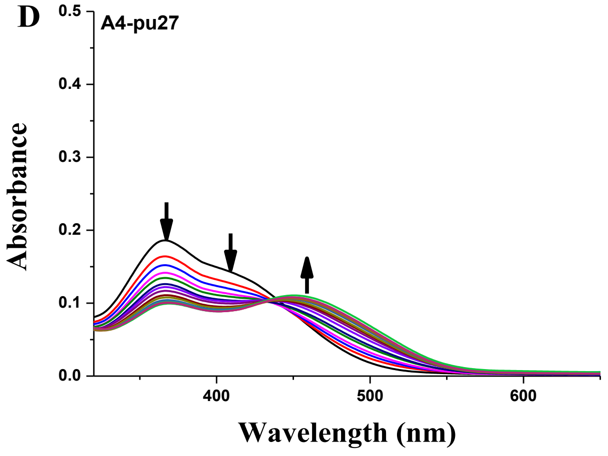
A4-pu27
Absorbance
0.0
0.1
0.2
0.3
0.4
0.5
400
500
600
Wavelength (nm)

J

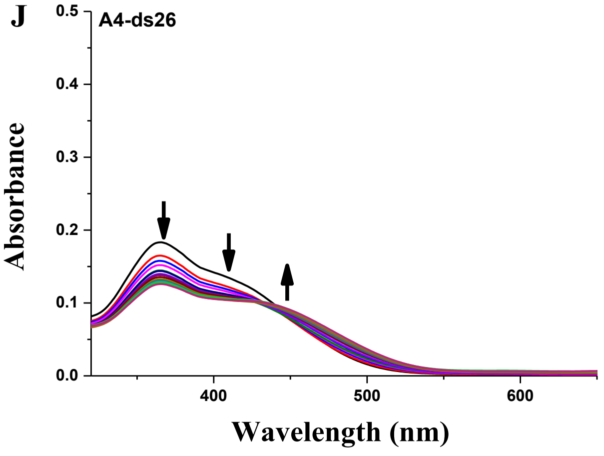
A4-ds26
Absorbance
0.0
0.1
0.2
0.3
0.4
0.5
400
500
600
Wavelength (nm)

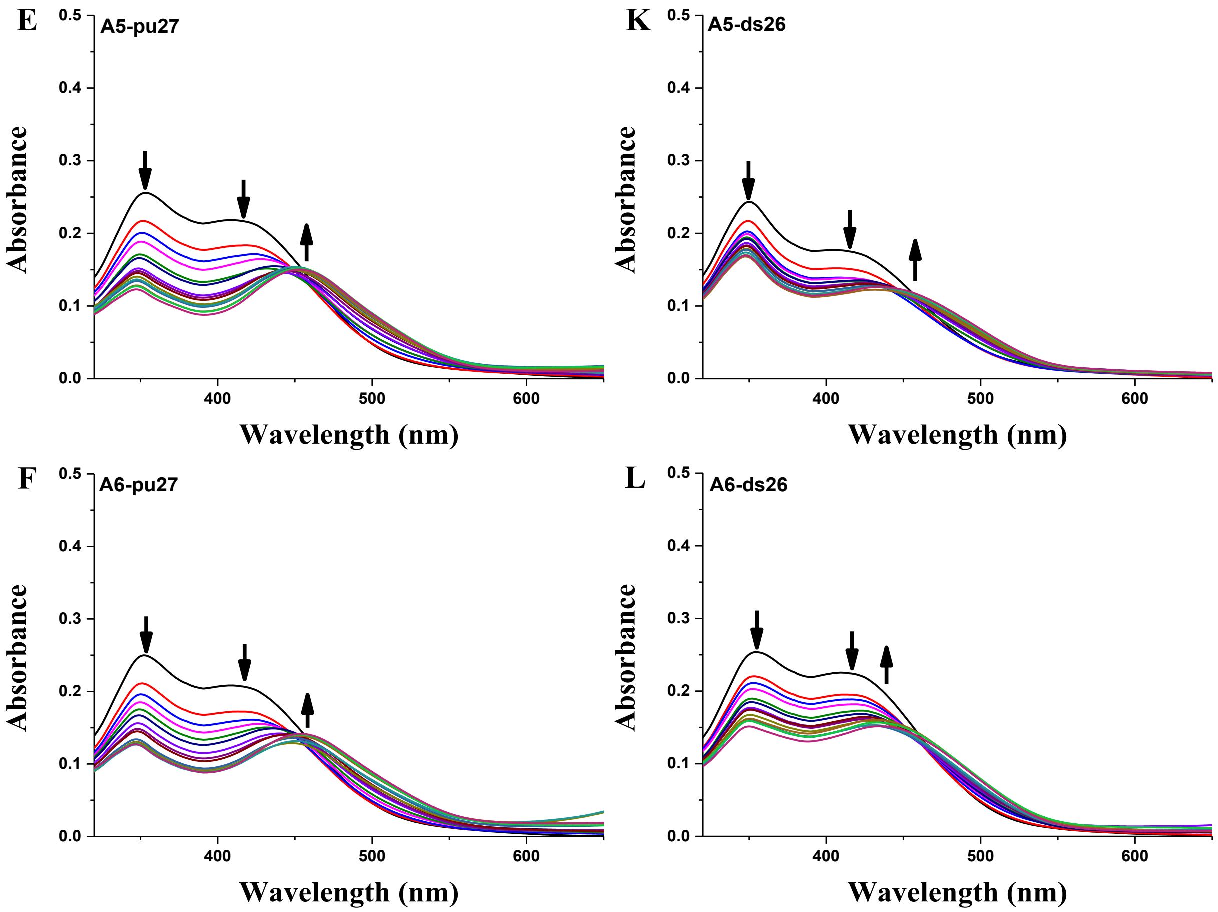

Fig. S14 UV-vis titration spectra of the probes **A1-A6** with pu27 or ds26 in a Tris-HCl buffer (10 mM, pH = 7.4). The concentration of the probes **A1-A6** used was 15 μM.

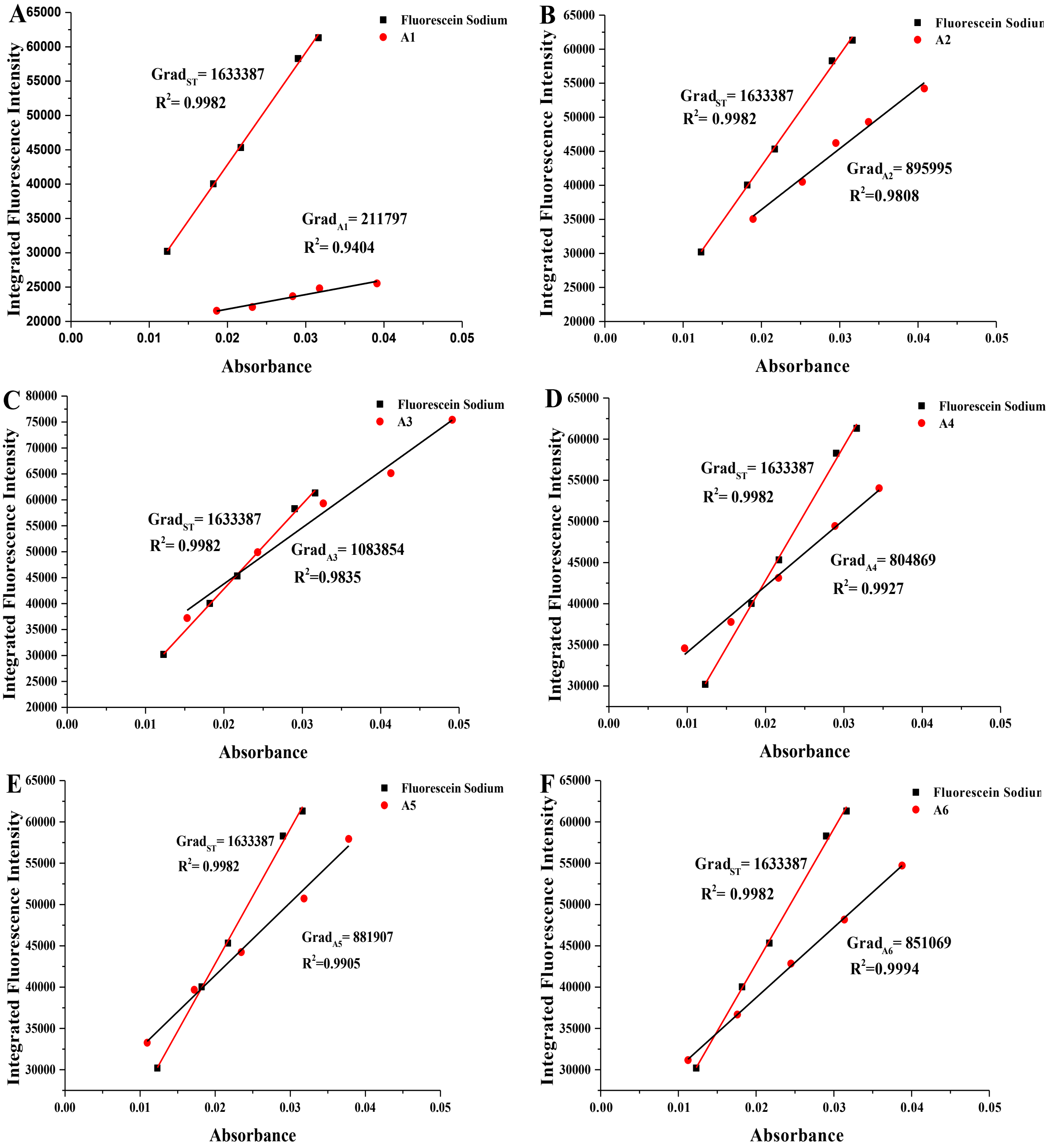

Fig. S15 The linear fitting of the absorption intensity by the fluorescence emission spectral integral area of the probes **A1-A6** and fluorescein sodium in pu27.

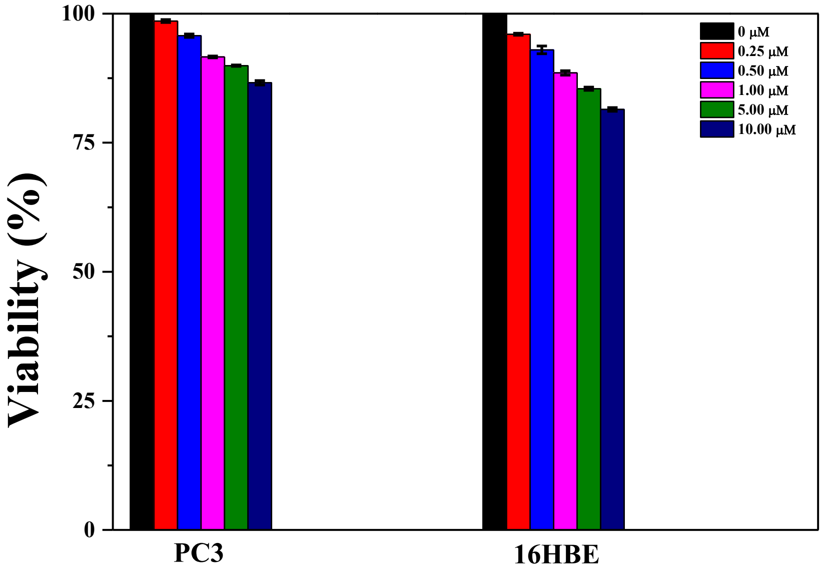

Fig. S16 Cells survival viability of PC3 cells and 16HBE cells in probe **A3** at concentrations of 0, 0.25, 0.50, 1.00, 5.00 and 10.00 μM, respectively.

By MTT test, we found that probe **A3** was low in toxicity against PC3 cancer cell and normal cell 16HBE. The cytotoxicity results were shown in **Fig. S15** When the concentration of **A3** was 10 μM, the survival viability of PC3 cells was 86.6 % and for 16HBE cells was 81.4 %. The estimated IC_{50} of **A3** in PC3 cells and 16HBE cells were found to be 54.44 μM and 35.64 μM, respectively. The low toxicity of **A3** may indicate that the fluorescent probe can be utilized in live cell experiments without interfering with cell growth or causing cell death, which is particularly useful for experiments require long-time video monitoring the bio-functions of G4-DNA in live cells.

Table S3. The comparison of red fluorescent probe **A3** with the recently reported analytical systems targeting G4-DNA substrates.

Probe	Selectivity	λ_{ex} (nm)	λ_{em} (nm)	Stokes shift	F/F_0[1]	Binding constant	LOD[4] (nM)	In cellulo imaging
9CI [1]	c-MYC G4-DNA	405	472	67	—	—	—	A549 cells and HepG2 cells
IZNP-2 [2]	Parallel G4-DNA	450	520	70	220	K_D[2] = 1.5 μmol	—	—
IZFL-2 [3]	c-MYC G4-DNA	450	520	70	10-14	K_D[2] = 0.53 μmol	—	—
L-1 [4]	c-MYC G4-DNA	463	587	124	600	K_a[3] = 18.8×10^5 M^{-1}	0.96	HepG2 cells
NCT [5]	Mitochondrial G4-DNA	466	650	184	110-250	—	3.1-8.7	Hela cells
Ls-2 [6]	G4-DNA	480	630	150	—	K_a[3] = 4.1×10^5 M^{-1} - 22.2×10^5 M^{-1}	8.8-37.7	HepG2 cells
CZ-BT [7]	Telomere G4-DNA	460	580	120	22	—	15.6	COS7 cells and MCF-7 cells
IMT [8]	G4-DNA	415	500	85	259-630	—	—	Hela cells[5]
TO-BTZ [9]	Telomere G4-DNA	450	550	100	45	K_D[2] = 6 μmol	—	SiHa cells
1 [10]	G4-DNA	405	510	105	20-30	K_a[3] = 1.53×10^5 M^{-1}	52.22	L929 cells
A3 (this work)	G4-DNA	498	610	112	30-70	K_a[3] = 16.67×10^5 M^{-1}	4.0	PC3 cells[5]

[1] F_0 represents the fluorescence intensity without G4-DNA and F represents the fluorescence intensity after adding G4-DNA.

[2] Dissociation constants.

[3] Apparent binding constants.

[4] Limit of G4-DNA detection.

[5] Co-localization of probe with BG4 antibody.

3. Reference

[1] Q. Q. Zhai, C. Gao, J. Q. Ding, Y. S. Zhang, B. Islam, W. X. Lan, H. T. Hou, H. Deng, J. Li, Z. Hu, H. I. Mohamed, S. Z. Xu, C. Y. Cao, S. M. Haider, D. G. Wei, Selective recognition of c-MYC Pu22 G-quadruplex by a fluorescent probe, Nucleic Acids Res. 47 (2019) 2190 - 2204.

[2] M. H. Hu, X. Chen, J. H. Tan, Development of a multitasking fluorescent probe for differentiating G-quadruplex structures, Dyes Pigments. 170 (2019) 107560.

[3] M. H. Hu, J. W. Zhou, W. H. Luo, S. B. Chen, Z. H. Huang, R. B. Wu, J. H. Tan, Development of a smart fluorescent sensor that specifically recognizes the c-MYC G-quadruplex, Anal. Chem. 91 (2019) 2480 - 2487.

[4] M. H. Wang, Y. Zhang, X. Y. Zeng, H. Yang, R. Y. Fu, H. J. Li, A benzo(f)quinolinium fused chromophore-based fluorescent probe for selective detection of c-myc G-quadruplex DNA with a red emission and a large Stocks shift, Dyes Pigments. 168 (2019) 334 - 340.

[5] L. L. Li, H. R. Xu, K. Li, Q. Yang, S. L. Pan, X. Q. Yu, Mitochondrial G-quadruplex targeting probe with near-infrared fluorescence emission, Sens. Actuators B. 286 (2019) 575 - 582.

[6] M. Q. Wang, J. Xu, L. Zhang, Y. Liao, H. Wei, Y. Y. Yin, Q. Liu, Y. Zhang, , Tuning the selectivity of N-alkylated styrylquinolinium dyes for sensing of G-quadruplex DNA, Bioorg. Med. Chem. 27 (2019) 552 - 559.

[7] F. L. Gao, S. H. Cao, W. Sun, S. Long, J. L. Fan, X. J. Peng, Development of a two-photon carbazole derivative probe for fluorescent visualization of G-quadruplex DNA in cells, Dyes Pigments. 171 (2019) 107749.

[8] S. G. Zhang, H. X. Sun, L. X. Wang, Y. Liu, H. B. Chen, Q. Li, A. J. Guan, M. R. Liu, Y. L. Tang, Real-time monitoring of DNA G-quadruplexes in living cells with a small-molecule fluorescent probe, Nucleic Acids Res. 46 (2018) 7522 - 7532.

[9] Y. Q. Wang, M. H. Hu, R. J. Guo, S. B. Chen, Z. S. Huang, J. H. Tan, Tuning the selectivity of a commercial cyanine nucleic acid dye for preferential sensing of hybrid telomeric G-quadruplex DNA, Sens. Actuators B. 266 (2018) 187 - 194.

[10] N. Sun, C. Wang, M. H. Xu, Y. J. Lu, Y. Y. Zheng, Y. Yan, X. L. Xiao, J. Q. Hou, K. Zhang, L. G. Luyt, W. L. Wong, C. F. Chow, The interaction of a structural flexible small molecule with nucleic acid structures: Investigation of the origin of fluorescence signal discrimination in sensing and the utilization in live cell imaging, Sens. Actuators B 250 (2017) 543 - 551.